SIAM J. SCI. COMPUT.
Vol. 24, No. 4, pp. 1232–1266

DIRECT RECONSTRUCTIONS OF CONDUCTIVITIES FROM BOUNDARY MEASUREMENTS*

JENNIFER L. MUELLER† AND SAMULI SILTANEN‡

Abstract. The problem of reconstructing an unknown electric conductivity from boundary measurements has applications in medical imaging, geophysics, and nondestructive testing. A. Nachman [*Ann. of Math.* (2), 143 (1996), pp. 71–96.] proved global uniqueness for the two-dimensional inverse conductivity problem using a constructive method of proof. Based on this proof, Siltanen, Mueller, and Isaacson [*Inverse Problems*, 16 (2000), pp. 681–699] presented a new numerical reconstruction method that solves the nonlinear problem directly without iteration. The method was verified with nonnoisy rotationally symmetric examples. In this paper the method is extended by introducing a new regularization scheme, which is analyzed theoretically and tested on symmetric and nonsymmetric numerical examples containing computer simulated noise.

Key words. inverse conductivity problem, electrical impedance tomography, exponentially growing solution, Faddeev's Green's function, scattering transform, $\bar{\partial}$ equation

AMS subject classification. 15

PII. S1064827501394568

1. Introduction.

The two-dimensional (2-D) inverse conductivity problem consists of determining an unknown conductivity distribution inside a bounded region $\Omega \subset \mathbb{R}^2$ from knowledge of the Dirichlet-to-Neumann, or voltage-to-current, map. The inverse conductivity problem has applications in subsurface flow monitoring and remediation [25, 27, 56, 64], underground contaminant detection [26, 57], nondestructive evaluation [30, 77, 78], and a medical imaging technique known as electrical impedance tomography (EIT) (see [24] for a review article on EIT). In EIT the domain Ω is often a cross-section of the body, such as a patient's chest. The tissues and organs in the body have different conductivities, a fact which enables one to form an image from the conductivity distribution $\gamma(x)$. By applying a basis of current patterns on electrodes attached around the patient's chest and measuring the resulting voltages on the electrodes, the solution to the inverse conductivity problem yields a 2-D image of a cross-section of the chest. In this geometry, several of the clinical applications include monitoring heart and lung function, diagnosis of pulmonary embolis (a blood clot in the lung), diagnosis of pulmonary edema, monitoring for internal bleeding, and the early detection of breast cancer.

The inverse conductivity problem is modeled by the generalized Laplace equation

$$\nabla \cdot \gamma \nabla u = 0 \quad \text{in } \Omega, \tag{1}$$

where $u(x)$ represents the electric potential and $\gamma(x)$ represents the conductivity. Applying a known voltage on the boundary of the region $\Omega \subset \mathbb{R}^n, n \geq 2$, corresponds

*Received by the editors August 29, 2001; accepted for publication (in revised form) September 2, 2002; published electronically February 6, 2003. The numerical calculations in this paper were performed using computing equipment supported in part by NSF cooperative agreement ACI-9619020 through computing resources provided by the National Partnership for Advanced Computational Infrastructure at the San Diego Supercomputer Center.

http://www.siam.org/journals/sisc/24-4/39456.html

†Department of Mathematics, Colorado State University, Fort Collins, CO 80523 (mueller@math.colostate.edu). The research of this author was supported by the NSF under grant DMS-0104861.

‡Instrumentarium Corp. Imaging Division, P.O. Box 20, FIN-04301 Tuusula, Finland (samuli.siltanen@fi.instrumentarium.com).

to the Dirichlet boundary condition

$$u = f \quad \text{on } \partial\Omega, \tag{2}$$

and knowledge of the resulting current density distribution gives rise to the Neumann boundary condition

$$\gamma \frac{\partial u}{\partial \nu} = g \quad \text{on } \partial\Omega. \tag{3}$$

Thus, the physical interpretation of the Dirichlet-to-Neumann map Λ_γ is knowledge of the resulting current distributions on the boundary of Ω corresponding to all possible voltage distributions on the boundary.

The uniqueness question is to determine whether γ is uniquely determined by Λ_γ. The reconstruction problem is how to obtain γ from the knowledge of Λ_γ. This is a difficult problem partly because the map $\Lambda_\gamma \mapsto \gamma$ is nonlinear. Moreover, the reconstruction problem is ill-posed in the sense that large changes in the conductivity can correspond to small changes in the boundary data. Furthermore, the problem is more difficult in dimension $n = 2$ than $n \geq 3$. One way to see this formally is simply to count degrees of freedom. In $\mathbb{R}^n$, the Dirichlet-to-Neumann data contain $2(n-1)$ variables, while the conductivity consists of n unknowns. Hence in $n = 2$ the problem is formally determined, while in $n \geq 3$ it is overdetermined.

We briefly review theoretical results on the inverse conductivity problem. Motivated by geophysical applications, in 1980 Calderón [20] showed how to determine nearly constant conductivities from the Dirichlet-to-Neumann map. His proof made use of the complex exponential harmonic functions $u = e^{x\cdot\rho}$ and $v = e^{-x\cdot\bar{\rho}}$, where $\rho \in \mathbb{C}^n$ and $\rho\cdot\rho = 0$ (here and throughout $\cdot$ denotes the vector dot product). This approach motivated the use of special complex exponentially growing solutions in later work on the inverse conductivity problem.

A uniqueness result on the boundary was proved by Kohn and Vogelius [44] in 1984. They showed that the Dirichlet-to-Neumann map Λ_γ uniquely determines $\frac{\partial^k \gamma}{\partial \nu}|_{\partial\Omega}$ for all $k \geq 0$ and $\gamma \in \mathbb{C}^\infty(\bar{\Omega})$. In [45] they proved the interior result that if $\partial\Omega$ is C^∞ and γ is piecewise analytic, then Λ_γ determines γ uniquely in dimensions $n \geq 2$. The continuous dependence of $\gamma|_{\partial\Omega}$ on Λ_γ is given in [73].

In [72] Sylvester and Uhlmann showed that if $\partial\Omega$ is C^∞, then Λ_γ uniquely determines $\gamma \in C^\infty(\bar{\Omega})$ in dimensions $n \geq 3$. Their smoothness assumption on γ was relaxed to $\gamma \in W^{2,\infty}(\Omega)$ in [54], and $\partial\Omega \in C^{1,1}$ in [51], and $\partial\Omega$ Lipschitz in [4]. A logarithmic continuous dependence result of γ on Λ_γ is given in [3]. The global uniqueness result in $\mathbb{R}^n$, $n \geq 3$, was then extended to a larger class of PDEs in [36]. Nachman gave a reconstruction method in [51] in dimensions $n \geq 3$ for $\gamma \in C^{1,1}$ with $\partial\Omega \in C^{1,1}$. For generalizations of the above results to more general spaces and other related work, see the references given in [74, 52, 38].

Local uniqueness results in two dimensions for nearly constant conductivities are found in [65, 67, 71]. The global uniqueness question in two dimensions remained open until 1996, when it was resolved for $\partial\Omega$ Lipschitz and $\gamma \in W^{2,p}(\Omega)$, $p > 1$, by Nachman [52]. This result was sharpened in 1997 to $W^{1,p}(\Omega)$, $p > 2$, conductivities by Brown and Uhlmann [19]. Stability analysis for these global uniqueness proofs are given in [47, 9]. Global uniqueness results under more restrictive hypotheses are found in [67, 70, 66]. For uniqueness results on Schrödinger operators, see [39, 21, 50].

In addition to the theoretical research, much work has been done in designing practical reconstruction algorithms for the inverse conductivity problem in $\mathbb{R}^2$ and $\mathbb{R}^3$. Existing algorithms can be categorized as follows:

1. noniterative linearization-based algorithms,
2. iterative algorithms solving the full nonlinear problem,
3. layer-stripping algorithms.

Linearization-based algorithms are based on the premise that the conductivity distribution is a small perturbation from a known, often constant, conductivity. Examples of linearization-based algorithms include backprojection methods [7, 8, 14, 58], Calderón's approach [20, 22, 35], moment methods [5], and one-step Newton methods [15, 48, 49, 23], which linearize about the constant conductivity determined to be the best fit to the measured data. However, the basic premise that the conductivity variations are small is often incorrect in applications. For example, the average conductivity of the lungs is 0.4 mS/cm during inspiration and 1 mS/cm during expiration—a significant difference. Breast tumors are known to be two to four times more conductive than healthy breast tissue [68, 69], and accurate conductivity values are needed to distinguish between benign and malignant lesions.

Algorithms solving the full nonlinear problem have been iterative in nature, with the exception of layer-stripping [63, 70]. These iterative algorithms have been based on output least-squares [16, 17, 28, 29, 41, 42, 79], the equation-error formulation [43, 46, 76], high contrast asymptotic theory [18], or statistical inversion [40]. While these approaches are promising for obtaining accurate reconstructed conductivity values, they may be slow to converge. All rely on regularization, either in the minimization functional or in the grid, since without regularization the reconstructed values will have large oscillations. This results in smoothing of the approximation, which may blur features and boundaries.

The theoretical and practical research traditions described above have seldom borrowed ideas from each other. However, the 2-D global uniqueness proof of Nachman [52] outlines a direct method for reconstructing γ without iteration. A practical algorithm based on Nachman's proof was introduced in [59] under the assumptions that $\partial\Omega$ is smooth, $\gamma \in C^2(\Omega)$, and $\gamma \equiv 1$ near the boundary. This method represents a new class of algorithm for EIT. It solves the full nonlinear problem, so it has the potential of reconstructing the conductivity values with high accuracy.

In this paper we present a regularized version of the reconstruction method given in [59], extend the method to more complicated conductivity distributions, and study the reconstructions from truncated scattering transforms.

Nachman's proof is divided into two steps:

$$\Lambda_\gamma \xrightarrow{1} \mathbf{t} \xrightarrow{2} \gamma,$$

where the intermediate object $\mathbf{t} : \mathbb{C} \to \mathbb{C}$ is called the (*nonphysical*) *scattering transform*, not directly measurable in experiments. It is remarkable that both steps consist of solving a linear integral equation although the full problem is nonlinear. This is possible since the proof is based on the $\bar\partial$ method of inverse scattering [13, 55]. The $\bar\partial$ method was first used by Beals and Coifman [10, 11] for the quantum inverse scattering problem in one dimension and was extended to 2-D problems in [1]. In the context of inverse scattering, the method leads to linear integral equations for reconstructing the eigenfunctions and the potential and also provides necessary conditions which the scattering data must satisfy. See also the references [12, 32, 53] for applications to multidimensional problems.

The paper is organized as follows. Section 2 gives an outline of Nachman's proof and the numerical reconstruction algorithm. In section 3 we present three numerical algorithms for the scattering transform. One of these is a new fast algorithm for the direct problem (i.e., when γ is known) and the others are for computing $\mathbf{t}$ approxi-

mately from boundary data. Combining either of these approximate algorithms with truncation of $\mathbf{t}$ leads to a regularized inversion algorithm for electrical impedance tomography. In section 4 we present new results about properties of $\bar\partial$ inversion: we derive an improved algorithm for solving the $\bar\partial$ equation numerically, show how symmetries in the (approximate) scattering transform show up in reconstructed conductivities, and prove a convergence theorem for truncating the scattering transform before $\bar\partial$ inversion. Section 5 contains numerical examples: radial ones containing computer simulated noise and nonsymmetric ones without noise.

2. The reconstruction method. We give a brief introduction to Nachman's proof and its numerical implementation; for more details see [52, 59, 60, 61, 62].

Let $\Omega \subset \mathbb{R}^2$ be the unit disc. According to section 6 of [52], we do not essentially lose generality with this assumption. Let $\gamma \in C^2(\Omega)$. We assume that $0 < c \le \gamma(x)$ for all $x \in \Omega$ and that $\gamma \equiv 1$ in a neighborhood of $\partial\Omega$.

The weak-form definition of the Dirichlet-to-Neumann map is given by

$$\Lambda_\gamma : H^{1/2}(\partial\Omega) \to H^{-1/2}(\partial\Omega), \qquad \langle \Lambda_\gamma f, g\rangle = \int_\Omega \gamma \nabla u \cdot \nabla v, \tag{4}$$

where v is any $H^1(\Omega)$ function with trace g on the boundary and u is the unique $H^1(\Omega)$ solution of the Dirichlet problem (1), (2).

The change of variables $q = \gamma^{-1/2}\Delta\gamma^{1/2}$ and $\tilde u = \gamma^{1/2}u$ transforms the conductivity equation (1) to the Schrödinger equation $(-\Delta + q)\tilde u = 0$ in Ω. Our assumption that γ be one near $\partial\Omega$ allows us to smoothly extend $\gamma = 1$ and $q = 0$ outside Ω. Special solutions ψ of the equation

$$(-\Delta + q)\psi(\cdot, k) = 0 \qquad \text{in } \mathbb{R}^2 \tag{5}$$

first introduced by Faddeev [31] are the key to the reconstruction. By Theorem 1.1 of [52] for any $k \in \mathbb{C} \setminus 0$, there is a unique solution ψ of (5) satisfying

$$e^{-ikx}\psi(x, k) - 1 \in W^{1,p} \tag{6}$$

for any $2 < p < \infty$. We use the complex notation $kx = (k_1 + ik_2)(x_1 + ix_2)$. The space $W^{1,p} = W^{1,p}(\mathbb{R}^2)$ is a special case of the definition $W^{m,\rho}(E) = \{f \in L^\rho(E) \,|\, \partial^\alpha f \in L^\rho(E),\ |\alpha| \le m\}$ for an arbitrary domain $E \subset \mathbb{R}^n$ and $1 \le \rho \le \infty$, $m \ge 0$; see [2].

The solutions ψ of (5) are constructed via the definition

$$\mu(x, k) := e^{-ikx}\psi(x, k), \qquad x \in \mathbb{R}^2,\ k \in \mathbb{C} \setminus 0. \tag{7}$$

The functions μ are the unique solutions of the Lippmann–Schwinger-type equation

$$\mu = 1 - g_k * (q\mu) \tag{8}$$

satisfying $\mu - 1 \in W^{1,p}$, where $*$ denotes convolution. Note that since $p > 2$, the Sobolev imbedding theorem implies that $\mu(\cdot, k)$ is a continuous function asymptotically close to 1. The function g_k appearing in (8) is given (in the sense of tempered distributions) by

$$g_k(x) := \frac{1}{(2\pi)^2} \int_{\mathbb{R}^2} \frac{e^{ix\cdot\xi}}{|\xi|^2 + 2k(\xi_1 + i\xi_2)} d\xi, \qquad (-\Delta - 4ik\bar\partial)g_k = \delta, \tag{9}$$

where $\bar\partial = (\partial/\partial x_1 + i\partial/\partial x_2)/2$. Accurate numerical algorithm for $g_k(x)$ is described in [59, 62, 34]. In section 3.1 of this paper we present a new fast method for numerical solution of μ from (8).

Define the scattering transform by

$$\mathbf{t}(k) := \int_{\mathbb{R}^2} e_k(x)q(x)\mu(x,k)dx, \qquad k \in \mathbb{C} \setminus 0, \tag{10}$$

where the exponential function e_k satisfying $|e_k(x)| = 1$ is defined by

$$e_k(x) := e^{i(kx+\bar{k}\bar{x})} = e^{-i(-2k_1,2k_2)\cdot x}. \tag{11}$$

Note that since μ is asymptotically close to 1, the scattering transform $\mathbf{t}$ is approximately the Fourier transform of q. Indeed, by the proof of Lemma 2.6 of [52] we have for some $-1 < s < 0$ and large $|k|$ the inequality

$$|\mathbf{t}(k_1,k_2) - \hat{q}(-2k_1,2k_2)| \leq C|k|^s. \tag{12}$$

In addition to (12), there are qualitative similarities between $\mathbf{t}$ and $\hat{q}$. It was proved in Theorem 3.3 of [59] that, roughly, (i) $\mathbf{t}$ is radial if and only if γ is radial, (ii) dilating the conductivity by $\gamma(\lambda x)$ for some $\lambda > 0$ corresponds to dilating the scattering transform by $\mathbf{t}(k/\lambda)$, (iii) reflectional symmetry in γ corresponds to reflectional symmetry in $\mathbf{t}$, and (iv) translating γ corresponds to multiplication of $\mathbf{t}$ by certain exponential function of modulus one. Moreover, it was proved in Theorem 3.2 of [59] that extra smoothness in γ allows stronger decay estimates for $\mathbf{t}$ at infinity.

We present the two main steps of Nachman's proof.

Step 1 *(from* Λ_γ *to* $\mathbf{t}$*).* Define a single-layer operator S_k for $k \in \mathbb{C} \setminus 0$ by

$$(S_k\phi)(x) := \int_{\partial\Omega} G_k(x-y)\phi(y)d\sigma(y). \tag{13}$$

The kernel G_k of S_k is Faddeev's Green's function

$$G_k(x) := e^{ikx}g_k(x), \qquad -\Delta G_k = \delta, \tag{14}$$

where g_k is given by (9). Denote the Dirichlet-to-Neumann map of the homogeneous conductivity 1 by Λ_1. By Theorem 5 of [52] the integral equation

$$\psi(\cdot,k)|_{\partial\Omega} = e^{ikx} - S_k(\Lambda_\gamma - \Lambda_1)\psi(\cdot,k) \tag{15}$$

is a Fredholm equation of the second kind and uniquely solvable in $H^{1/2}(\partial\Omega)$ for any $k \in \mathbb{C} \setminus 0$. Furthermore, $\mathbf{t}$ can be recovered from the formula

$$\mathbf{t}(k) = \int_{\partial\Omega} e^{i\bar{k}\bar{x}}(\Lambda_\gamma - \Lambda_1)\psi(\cdot,k)d\sigma. \tag{16}$$

The numerical solution of (15) is not stable if the data are noisy. We present in section 3 two alternative methods for computing the scattering transform from boundary data. The methods are robust for small and moderately large $|k|$. In method (a) we make (15) less sensitive to errors in Λ_γ by replacing S_k by S_0. The resulting approximations to ψ on $\partial\Omega$ are then used in (16). In method (b) we replace ψ on $\partial\Omega$ by its asymptotic limit e^{ikx} in (16). In either case, we truncate the numerical approximation to $\mathbf{t}(k)$ at some radius $|k| = R > 0$ before using it in the $\bar{\partial}$ inversion of Step 2. In Theorem 4.2 of this paper we show that reconstructions from truncations of the exact scattering transform converge pointwise to the true conductivity.

Truncating either of the approximations can be viewed as a regularization scheme in the sense that it provides stable approximate computation of $\mathbf{t}$.

Step 2 *(from* $\mathbf{t}$ *to* γ*).* Theorem 2.1 of [52] implies that the $\bar\partial$ equation

$$\frac{\partial}{\partial \bar k}\mu(x,k) = \frac{1}{4\pi \bar k}\mathbf{t}(k)e_{-k}(x)\overline{\mu(x,k)}, \qquad k \neq 0, \tag{17}$$

holds where $e_{-k}(x)$ is defined in (11), and Theorem 4.1 of [52] shows that (17) is uniquely solvable. Note that differentiation in (17) is carried out with respect to the complex spectral parameter k. For any fixed $x \in \mathbb{R}^2$, the solution satisfies

$$\mu(x,k) = 1 + \frac{1}{(2\pi)^2}\int_{\mathbb{R}^2} \frac{\mathbf{t}(k')}{(k-k')\bar{k'}} e_{-x}(k')\overline{\mu(x,k')}dk_1'dk_2' \tag{18}$$

for all $k \in \mathbb{C} \setminus 0$. Note that the integral is taken over the k-plane, so to solve (18) $\mu(x,k)$ is needed for all values of $k \in \mathbb{C} \setminus 0$. Once solved from (18), the functions $\mu(x,k)$ can be used to recover γ [52, section 3]:

$$\gamma^{1/2}(x) = \lim_{k\to 0}\mu(x,k). \tag{19}$$

The stability analysis of Liu [47] shows that Step 2 has linear stability whereas Step 1 has only logarithmic stability. Inspired by Liu's results, we choose not to regularize Step 2. We discuss the numerical solution of (18) in section 4.1.

In Theorem 4.1 we show that certain symmetries in the approximate scattering transform used in (18) result in symmetries in the reconstruction.

3. Numerical approximations to the scattering transform. We compute $\mathbf{t}$ for given conductivities by solving the Lippmann–Schwinger equation (8) for μ and substituting the result into the definition of $\mathbf{t}$, to which we then apply a numerical quadrature technique. We call the result of this computation $\mathbf{t}^{\text{LS}}$ and present the details in section 3.1.

Ultimately we wish to reconstruct conductivities from noisy boundary data. In section 3.2 we explain how we simulate noisy measurements in this study.

We present two methods for computing $\mathbf{t}$ from Λ_γ. Method (a): Solve the (regularized) boundary integral equation (15) numerically and substitute the solutions $\psi^B \approx \psi$ into formula (16). We will call the result of this computation $\mathbf{t}^{\text{B}}$ when the data are not noisy and $\tilde{\mathbf{t}}^{\text{B}}$ when the data are noisy. The details are presented in section 3.3. Method (b): Replace ψ by e^{ikx} in (16). We will call the result of this computation $\mathbf{t}^{\text{exp}}$ when the data are not noisy and $\tilde{\mathbf{t}}^{\text{exp}}$ when the data are noisy. See section 3.4 for details.

3.1. Computing t for given conductivities: $\mathbf{t}^{\text{LS}}$. To compute $\mathbf{t}$ numerically we solve first the Lippmann–Schwinger equation (8) to find numerical approximations μ^{LS} of μ for test conductivities. Our solution algorithm for (8) is a modification of the method introduced by Vainikko in section 2 of [75] for the Lippmann–Schwinger equation related to the Helmholtz equation. A slightly more general version of the algorithm for exponentially growing solutions will be given in [34]. Vainikko's method and its modifications have computational complexity $M^2 \log M$ when the solutions are computed on a $M \times M$ grid. The complexity of the earlier scattering transform computation described in [59] is M^4.

Fix $k \in \mathbb{C} \setminus 0$. Following Vainikko, write (8) in the form

$$[I + g_k * (q\cdot\ )]w = 1. \tag{20}$$

We verify that Vainikko's assumptions hold. By [52] we have unique solvability of (20) for all $k \neq 0$. All functions (apart from g_k) that we evaluate on the grid are continuous. Finally, Vainikko treats (20) with a fundamental solution for the Helmholtz equation as the kernel. The fundamental solution g_k that we use has a logarithmic singularity at the origin and is otherwise smooth. Thus replacing the fundamental solution by g_k is justified.

Let us describe the algorithm. Choose such an $S > 0$ that $\mathrm{supp}(q) \subset [-S, S]^2 \subset \mathbb{R}^2$. Choose a positive integer m, denote $M := 2^m$, and set $h := 2S/M$. We define the grid approximation for a continuous function φ by

$$\varphi_{j,h} = \varphi(jh), \qquad j \in \mathbb{Z}_m^2, \tag{21}$$

$$\mathbb{Z}_m^2 := \{j = (j_1, j_2) \in \mathbb{Z}^2 \mid -2^{m-1} \leq j_k < 2^{m-1},\ k = 1, 2\}. \tag{22}$$

Continuous functions are thus represented by $2^m \times 2^m$ matrices of function values on the grid points.

We require a discretized version of the convolution operator

$$(T\varphi)(x) = (g_k * \varphi)(x) = \int_{\mathbb{R}^2} g_k(x - y)\varphi(y)dy, \tag{23}$$

where $\mathrm{supp}(\varphi) \subset [-S, S]^2$. For this, set

$$g_{j,h} = \begin{cases} g_k(jh) & \text{for } j \in \mathbb{Z}_{m+1}^2 \setminus 0, \\ 0 & \text{for } j = 0, \end{cases} \tag{24}$$

and consider $\varphi_{\ell,h}$ as defined in (21). The discrete counterpart T_h of T is defined by

$$(T_h\varphi)_{j,h} = h^2 \sum_{\ell \in \mathbb{Z}_m^2} g_{j-\ell,h}\varphi_{\ell,h} \qquad \text{for } j \in \mathbb{Z}_m^2. \tag{25}$$

Formula (25) evaluates the continuous function $T\varphi$ at the grid points approximately; the approximation comes from implementing the integral in (23) as a simple quadrature and ignoring the integrable singularity of $g_k(x)$ at $x = 0$. The practical value of formula (25) is that application of T_h can be implemented using the FFT. Namely, introduce the zero-padded version of $\varphi_{k,h}$ as

$$\Phi = \left[\begin{array}{c|c} \varphi_{k,h} & 0_{M\times M} \\ \hline 0_{M\times M} & 0_{M\times M} \end{array}\right],$$

where $0_{M\times M}$ is an all-zero matrix of size $M \times M$. Then a fast implementation of T_h is achieved as a certain $M \times M$ submatrix of the matrix $h^2\mathrm{FFT}^{-1}[\mathrm{FFT}(g_{k,h})\mathrm{FFT}(\Phi)]$ (where this product is taken pointwise). Note that the FFT is applied to matrices of size $2^{m+1} \times 2^{m+1} = 2M \times 2M$, and thus the complexity of one application of T_h is $\mathcal{O}(M^2 \log M)$.

We can now write (20) in the form

$$[I + T_h(q_{j,h}\cdot\,)]w_{j,h} = f_{j,h}, \tag{26}$$

where $q_{j,h}\cdot$ denotes componentwise multiplication by $q_{j,h}$. Then, using an iterative solver (such as GMRES), we can solve (26).

The scattering transform $\mathbf{t}$ is computed with the midpoint rule:

$$\mathbf{t}^{\mathrm{LS}}(k) := h^2 \sum_{j \in \mathbb{Z}_m^2} e_k(jh)\mu^{\mathrm{LS}}(jh, k)q(jh). \tag{27}$$

3.2. Simulation of measurement noise. We introduce noise into the numerically simulated data by roughly modeling practical EIT measurements. In this study we consider radial examples for which we have Λ_γ available with great accuracy. We modify this accurate operator by simulating measurements. Note that in practice one works with the Neumann-to-Dirichlet map—currents are applied and voltages measured for stability reasons.

Assume that γ is radial. It is shown in [70] that

$$\Lambda_\gamma \phi_n = \lambda_n \phi_n, \qquad \phi_n(\theta) := (2\pi)^{-1/2} e^{in\theta}, \qquad n \in \mathbb{Z}. \tag{28}$$

Thus Λ_γ can be represented in the trigonometric basis by the collection $\{\lambda_n\}_{n=-\infty}^{\infty}$ of its (nonnegative) eigenvalues. The numerical approximation of the eigenvalues is described in [59].

We use a very crude electrode model by applying trigonometric voltage functions $\phi_n(\theta_j)$ at 32 equidistant points $\theta_0, \ldots, \theta_{31}$ on the unit circle for $n = -16, \ldots, 15$. The number of evaluation points is the same as the number of electrodes in the ACT3 impedance imaging system at Rensselaer Polytechnic Institute [24]. We simulate the current measurement corresponding to the voltage $\phi_n(\theta_j)$ by

$$\lambda_n \phi_n(\theta_j) + \varepsilon_j,$$

where λ_n is an accurate numerical approximation to the nth eigenvalue of Λ_γ and ε_j are independent Gaussian random variables with zero mean and standard deviation 0.0001. This is approximately the noise level of the ACT3 system. Using these noisy current values, we build a matrix representation of Λ_γ in the trigonometric basis.

3.3. Method (a) for computation of t from boundary data: $\mathbf{t}^{\mathrm{B}}$ and $\tilde{\mathbf{t}}^{\mathrm{B}}$. Let $G_0(x) := -(2\pi)^{-1} \log|x|$ be the standard Green's function for $-\Delta$. It was shown in [59, 60] that the Fredholm operator appearing in (15) can be written in the form

$$I + S_k(\Lambda_\gamma - \Lambda_1) = I + S_0(\Lambda_\gamma - \Lambda_1) + \mathcal{H}_k(\Lambda_\gamma - \Lambda_1), \tag{29}$$

where S_0 is the standard single-layer operator with kernel G_0 and $\mathcal{H}_k$ is an integral operator with smooth but exponentially growing kernel:

$$(\mathcal{H}_k \varphi)(x) = \int_{\partial\Omega} \tilde{H}_1(k(x-y)) \varphi(y) d\sigma(y), \tag{30}$$

where $\tilde{H}_1(x) := H_1(x) - H_1(0)$ and $H_1 := G_1 - G_0$ is the difference between Faddeev's Green function and the standard one. We drop the term in (29) containing $\mathcal{H}_k$ and solve for ψ^{B} from

$$\psi^{\mathrm{B}}(\cdot, k)|_{\partial\Omega} = e^{ikx} - S_0(\Lambda_\gamma - \Lambda_1)\psi^{\mathrm{B}}(\cdot, k). \tag{31}$$

This is possible since the operator

$$A_\gamma := I + S_0(\Lambda_\gamma - \Lambda_1) \tag{32}$$

is invertible in $H^{1/2}(\partial\Omega)$ [60]. We compute the approximation $\mathbf{t}^{\mathrm{B}}$ for $\mathbf{t}$ from the formula

$$\mathbf{t}^{\mathrm{B}}(k) = \int_{\partial\Omega} e^{i\bar{k}\bar{x}} (\Lambda_\gamma - \Lambda_1)\psi^{\mathrm{B}}(\cdot, k) d\sigma. \tag{33}$$

We explain how to compute $\mathbf{t}^{\mathrm{B}}$ in practice. We assume that Λ_γ is available as a possibly noisy matrix acting on the Fourier basis. The Dirichlet-to-Neumann map Λ_1 and Neumann-to-Dirichlet map R_1 corresponding to the homogeneous conductivity 1 have the following form in the trigonometric basis:

$$\Lambda_1\phi_n = |n|\phi_n, \qquad R_1\phi_n = |n|^{-1}\phi_n, \qquad n \in \mathbb{Z}\setminus 0. \tag{34}$$

In addition, $\Lambda_1\phi_0 = 0$, and $R_1\phi_0$ is not defined. When Ω is the unit disc we have the identity $2S_0 = R_1$; see [60]. We thus have a representation of the operator A_γ in the Fourier basis. Equation (31) can be solved with an iterative solver (such as GMRES).

It is possible to implement the operator (30) numerically and solve the original equation (15). However, with noisy data this computation is instable except for very small $|k|$. Numerical solution of (31) is feasible with noisy data for moderately large $|k|$ as will be demonstrated in section 5.

Is the approximation $\mathbf{t}^{\mathrm{B}}$ close to $\mathbf{t}$? Numerical examples presented in section 5 suggest so. Moreover, for k near zero we prove a pointwise estimate (Theorem 3.1) and as qualitative evidence we derive a symmetry result (Lemma 3.2) analogous to Theorem 3.3 in [59].

THEOREM 3.1. *Let $\Omega \subset \mathbb{R}^2$ be the unit disc. Let $\gamma \in C^2(\Omega)$ be a strictly positive conductivity equal to 1 near $\partial\Omega$. Define the corresponding scattering transform $\mathbf{t}$ by* (10) *and the approximate scattering transform $\mathbf{t}^{B}$ by* (31) *and* (33)*. Then for k near zero we have the estimate*

$$|\mathbf{t}(k) - \mathbf{t}^{B}(k)| \le C|k|^3. \tag{35}$$

Proof. The following integral equations hold in $H^{1/2}(\partial\Omega)$:

$$\begin{aligned}\psi - 1 &= e^{ikx} - 1 - S_k(\Lambda_\gamma - \Lambda_1)(\psi - 1),\\ \psi^{\mathrm{B}} - 1 &= e^{ikx} - 1 - S_0(\Lambda_\gamma - \Lambda_1)(\psi^{\mathrm{B}} - 1).\end{aligned}$$

Thus $\psi^{\mathrm{B}} - 1 = A_\gamma^{-1}(e^{ikx} - 1)$. It was shown in [59] that $\|\mathcal{H}_k\|_{L(H^{(1/2)})} \le C|k|$ for k near zero. Moreover, since $\gamma \equiv 1$ near $\partial\Omega$, the operator $\Lambda_\gamma - \Lambda_1$ is infinitely smoothing and in particular bounded from $H^{1/2}(\partial\Omega)$ to itself. For k near zero we have $\|A_\gamma^{-1}\mathcal{H}_k(\Lambda_\gamma - \Lambda_1)\|_{L(H^{(1/2)})} < 1$ and we can write

$$\begin{aligned}\psi - 1 &= [A_\gamma + \mathcal{H}_k(\Lambda_\gamma - \Lambda_1)]^{-1}(e^{ikx} - 1)\\ &= A_\gamma^{-1}(e^{ikx} - 1) - A_\gamma^{-1}\mathcal{H}_k(\Lambda_\gamma - \Lambda_1)[I + A_\gamma^{-1}\mathcal{H}_k(\Lambda_\gamma - \Lambda_1)]^{-1}(e^{ikx} - 1).\end{aligned}$$

Use $\|e^{ikx} - 1\|_{H^{1/2}(\partial\Omega)} \le C_\varepsilon|k|$ to get $\|\psi - \psi^{\mathrm{B}}\|_{H^{1/2}(\partial\Omega)} \le C|k|^2$. We can bound $|\mathbf{t}(k) - \mathbf{t}^{\mathrm{B}}(k)|$ for k near zero using the inequality

$$|\langle (e^{i\bar{k}\bar{x}} - 1), (\Lambda_\gamma - \Lambda_1)(\psi - \psi^{\mathrm{B}})\rangle| \le C\|e^{i\bar{k}\bar{x}} - 1\|_{H^{1/2}(\partial\Omega)}\|\psi - \psi^{\mathrm{B}}\|_{H^{1/2}(\partial\Omega)} \le C|k|^3. \qquad \square$$

LEMMA 3.2. *Let $\Omega \subset \mathbb{R}^2$ be the unit disc. Let $\gamma_1, \gamma_2 \in C^2(\Omega)$ be strictly positive conductivities equal to 1 near $\partial\Omega$. Define the corresponding approximate scattering transforms $\mathbf{t}_1^{B}, \mathbf{t}_2^{B}$ by* (31) *and* (33)*. Denote rotation of a complex number z by angle $\varphi \in \mathbb{R}$ by $z_\varphi := e^{i\varphi}z$. Then*

$$\gamma_2(x) = \gamma_1(x_{-\varphi}) \quad \forall x \in \mathbb{R}^2 \qquad \Rightarrow \qquad \mathbf{t}_2^{B}(k) = \mathbf{t}_1^{B}(k_\varphi) \quad \forall k \in \mathbb{C}, \tag{36}$$

$$\gamma_2(x) = \gamma_1(-\bar{x}) \quad \forall x \in \mathbb{R}^2 \qquad \Rightarrow \qquad \mathbf{t}_2^{B}(k) = \overline{\mathbf{t}_1^{B}(\bar{k})} \quad \forall k \in \mathbb{C}. \tag{37}$$

Proof. Denote by ρ_φ the operator $(\rho_\varphi f)(x) = f(x_\varphi)$. Note that $\langle f, \rho_{-\varphi} g\rangle = \langle \rho_\varphi f, g\rangle$ and that $\rho_\varphi e^{ikx} = e^{ikx_\varphi} = e^{ik_\varphi x}$. Since $2S_0 = R_1$ we know that trigonometric functions are eigenfunctions for S_0 and it follows that $S_0\rho_\varphi = \rho_\varphi S_0$. Assume that $\gamma_2(x) = \gamma_1(x_{-\varphi})$. Then $\Lambda_{\gamma_2} = \rho_{-\varphi}\Lambda_{\gamma_1}\rho_\varphi$ and we can write $I + S_0(\Lambda_{\gamma_2} - \Lambda_1) = \rho_{-\varphi}[I + S_0(\Lambda_{\gamma_1} - \Lambda_1)]\rho_\varphi$ to get the identity

$$\begin{aligned}\psi_2^{\mathrm{B}}(x,k) &= [I + S_0(\Lambda_{\gamma_2} - \Lambda_1)]^{-1} e^{ikx} \\ &= \rho_{-\varphi}[I + S_0(\Lambda_{\gamma_1} - \Lambda_1)]^{-1}\rho_\varphi e^{ikx} = \psi_1^{\mathrm{B}}(x_{-\varphi}, k_\varphi),\end{aligned}$$

and we can calculate

$$\begin{aligned}\mathbf{t}_2^{\mathrm{B}}(k) &= \langle e^{i\bar{k}\bar{x}}, (\Lambda_{\gamma_2} - \Lambda_1)\psi_2^{\mathrm{B}}(x,k)\rangle \\ &= \langle e^{i\bar{k}\bar{x}}, \rho_{-\varphi}(\Lambda_{\gamma_1} - \Lambda_1)\rho_\varphi\psi_1^{\mathrm{B}}(x_{-\varphi}, k_\varphi)\rangle \\ &= \langle e^{i\bar{k}_\varphi\bar{x}}, (\Lambda_{\gamma_1} - \Lambda_1)\psi_1^{\mathrm{B}}(x, k_\varphi)\rangle = \mathbf{t}_1^{\mathrm{B}}(k_\varphi).\end{aligned}$$

Denote by R the operator $(Rf)(x) = f(-\bar{x})$ and note that $\langle f, Rg\rangle = \langle Rf, g\rangle$. Assume that $\gamma_2(x) = \gamma_1(-\bar{x})$. Then $\Lambda_{\gamma_2} = R\Lambda_{\gamma_1}R$ and S_0 commutes with R so we can compute as above to get (37). ∎

3.4. Method (b) for computation of t from boundary data: $\mathbf{t}^{\exp}$ and $\tilde{\mathbf{t}}^{\exp}$. In [59] the following approximation to $\mathbf{t}$ was introduced:

$$\mathbf{t}^{\exp}(k) := \int_{\partial\Omega} e^{i\bar{k}\bar{x}}(\Lambda_\gamma - \Lambda_1)e^{ikx}\,d\sigma, \qquad k \in \mathbb{C}. \tag{38}$$

This approximation comes from substituting the approximation $\psi \approx e^{ikx}$ into formula (16). It is simpler to use $\mathbf{t}^{\exp}$ than $\mathbf{t}^{\mathrm{B}}$: We need only to apply the noisy boundary measurements once in (38) instead of twice in (31) and (33).

Is $\mathbf{t}^{\exp}$ close to $\mathbf{t}$? The method of proof of Theorem 3.1 leads only to an estimate $|\mathbf{t}(k) - \mathbf{t}^{\exp}(k)| \le C|k|^2$ for k near zero, which is not very useful since both $\mathbf{t}$ and $\mathbf{t}^{\exp}$ are bounded by $C|k|^2$ for k near zero. However, numerical experiments show that $\mathbf{t}^{\exp}$ is often close to $\mathbf{t}$ and that it is possible to get reasonable reconstructions of conductivities from $\mathbf{t}^{\exp}$. In addition we have the following result on symmetries of $\mathbf{t}^{\exp}$.

LEMMA 3.3. *Let $\Omega \subset \mathbb{R}^2$ be the unit disc. Let $\gamma_1, \gamma_2 \in C^2(\Omega)$ be strictly positive conductivities equal to 1 near $\partial\Omega$. Define $\mathbf{t}_j^{\exp}(k) = \langle e^{i\bar{k}\bar{x}}, (\Lambda_{\gamma_j} - \Lambda_1)e^{ikx}\rangle$ for $j = 1, 2$. Then*

$$\gamma_2(x) = \gamma_1(x_{-\varphi}) \quad \forall x \in \mathbb{R}^2 \qquad \Rightarrow \qquad \mathbf{t}_2^{\exp}(k) = \mathbf{t}_1^{\exp}(k_\varphi) \quad \forall k \in \mathbb{C}, \tag{39}$$

$$\gamma_2(x) = \gamma_1(-\bar{x}) \quad \forall x \in \mathbb{R}^2 \qquad \Rightarrow \qquad \mathbf{t}_2^{\exp}(k) = \overline{\mathbf{t}_1^{\exp}(\bar{k})} \quad \forall k \in \mathbb{C}. \tag{40}$$

Proof. Assume that $\gamma_2(x) = \gamma_1(x_{-\varphi})$. Analogously to the proof of Lemma 3.2, we compute

$$\begin{aligned}\mathbf{t}_2^{\exp}(k) &= \langle e^{i\bar{k}\bar{x}}, (\Lambda_{\gamma_2} - \Lambda_1)e^{ikx}\rangle = \langle e^{i\bar{k}\bar{x}}, \rho_{-\varphi}(\Lambda_{\gamma_1} - \Lambda_1)\rho_\varphi e^{ikx}\rangle \\ &= \langle \rho_\varphi e^{i\bar{k}\bar{x}}, (\Lambda_{\gamma_1} - \Lambda_1)e^{ik_\varphi x}\rangle = \langle e^{i\bar{k}_\varphi\bar{x}}, (\Lambda_{\gamma_1} - \Lambda_1)e^{ik_\varphi x}\rangle = \mathbf{t}_1^{\exp}(k_\varphi).\end{aligned}$$

As in the proof of Lemma 3.2, identity (40) is proved similarly to (39). ∎

It is simple to compute $\mathbf{t}^{\exp}$ numerically for rotationally symmetric conductivities with and without composition by a conformal map. We present formulas for both cases below.

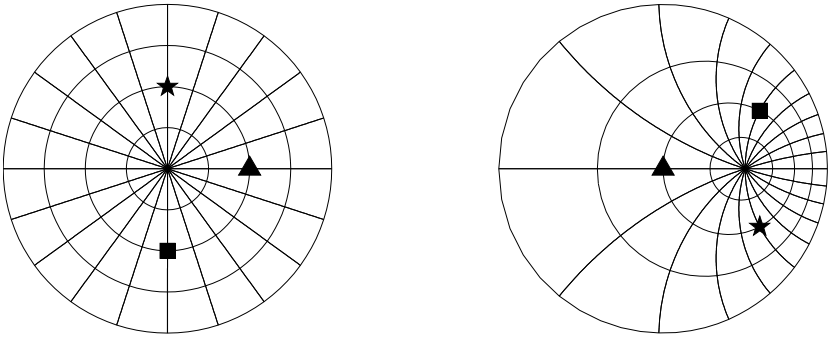

FIG. 1. *Action of the linear fractional transformation Ψ. The images of three points are marked for clarity. Note that $\Psi(\Omega) = \Omega$ and that $\Psi^{-1} = \Psi$.*

Assume rotational symmetry: $\gamma(x) = \gamma(|x|)$. Denote the eigenvalues of Λ_γ in the Fourier basis by $\{\lambda_n\}_{n=-\infty}^{\infty}$. Expand e^{ikx} as a Fourier series:

$$e^{ikx} = \sum_{n=-\infty}^{\infty} a_n(k) e^{in\theta} \quad \text{with} \quad a_n(k) = \begin{cases} \frac{(ik)^n}{n!}, & n \geq 0, \\ 0, & n < 0. \end{cases}$$

Substituting this series into formula (38) gives

$$\mathbf{t}^{\exp}(k) = \sum_{n=1}^{\infty} (\lambda_n - n) \frac{(-1)^n |k|^{2n}}{(n!)^2}. \tag{41}$$

Identify $\mathbb{C} = \mathbb{R}^2$ and define a map Ψ in a neighborhood of the closed unit disc $\overline{\Omega}$ by

$$\Psi(x) := \frac{x - 1/2}{x/2 - 1}, \qquad x = x_1 + ix_2; \tag{42}$$

see Figure 1. Then $\Psi \in \{(x-a)(\overline{a}x-1)^{-1}e^{i\theta} \,|\, a \in \mathbb{C}, |a| < 1, \theta \in \mathbb{R}\}$, the well-known class of conformal bijections $\overline{\Omega} \to \overline{\Omega}$ mapping $\partial\Omega$ onto itself. Therefore $\Psi(\Omega) = \Omega$. Moreover, Ψ is a Möbius transformation and maps circles in the interior of Ω to other such circles. The nonsymmetric conductivity $\tilde{\gamma}$ is then defined by $\tilde{\gamma} := \gamma \circ \Psi^{-1}$. To obtain the approximation $\mathbf{t}^{\exp}$ to $\mathbf{t}$ for these nonsymmetric examples, we proceed as in [33]. Write the conformal map Ψ as

$$\Psi(x) = \sum_{n=0}^{\infty} b_n x^n, \qquad b_0 = \frac{1}{2},\ b_n = -\frac{3}{2^{n+1}},\ n = 1, 2, 3, \ldots. \tag{43}$$

Then the approximate scattering transform corresponding to the conductivity $\tilde{\gamma}$ can be computed from

$$\mathbf{t}^{\exp}(k) = 2\pi \sum_{n=1}^{\infty} \overline{a_n(-ik)} a_n(ik)(\lambda_n - n), \tag{44}$$

where the functions $a_n(z)$ are given for complex z recursively by

$$a_0(z) = e^{b_0 z}, \qquad a_n(z) = \frac{z}{n} \sum_{l=0}^{n-1} (n-l) b_{n-l} a_l(z), \quad n = 1, 2, 3, \ldots. \tag{45}$$

4. From the scattering transform to the conductivity. To obtain the conductivity from the scattering transform, one must solve the $\bar{\partial}$ equation (17). In section 4.1 we present an improved numerical algorithm. However, in practical situations we are not given the actual scattering transform, but only a numerical approximation. In section 4.2 we discuss how symmetries in the approximate scattering transform manifest themselves in the reconstructed conductivities. In section 4.3 we prove that reconstructions from truncated (exact) scattering transforms converge pointwise to the correct conductivity when the cutoff radius grows.

4.1. Numerical solution of the $\bar{\partial}$ equation. To solve the $\bar{\partial}$ equation (17), we solve the weakly singular Fredholm integral equation of the second kind (18) for k in a bounded subset $R \subset \mathbb{C}$. In our implementation, R is a rectangle. The fact that the $\bar{\partial}$ equation must be solved independently for each x in the region of interest to obtain $\gamma(x)$ suggests the use of parallelization in a numerical method. We used the method developed in [59] with some small improvements, which we describe here.

Our $\bar{\partial}$-solver in [59] is a 2-D adaptation of the method of product integrals presented in [6]. The idea of the method is to factor the integrand into its smooth part and its singular part and approximate the smooth part with a simple function, such as an interpolatory polynomial. The new integrand is then computed analytically where possible. We stress that in the numerical solution of the $\bar{\partial}$ equation, no radial symmetry of γ or $\mathbf{t}$ was assumed.

Here we define a mesh $M = \{(u_j, v_i) : i, j = 0, \ldots, N+1\}$ on the rectangle R in such a way that $k = 0$ is not a mesh point. We approximate the function $f(x,k) := \frac{\mathbf{t}(k)}{\bar{k}} e_{-x}(k)\overline{\mu(x,k)}$ using bilinear interpolation, except on the mesh square Q_0 containing $k = 0$, and on the outermost squares in the mesh M, we set $\mu \equiv 1$, using the fact that $\mu \sim 1$. On the square Q_0, we use the fact that $\frac{\mathbf{t}(k)}{\bar{k}}|_{k=0} = 0$ and include a fifth interpolation point at the origin with $f(x,0) = 0$. This divides Q_0 into four triangles T_i, $i = 1,2,3,4$. On each triangle we approximate $f(x,k)$ by the plane through the two points on the corners of Q_0 and the origin. We denote the interpolant of $f(x,k)$ by $[f(x,k_1,k_2)]_{ji}$, where this notation represents the planar interpolant on T_i and the bilinear interpolant on all squares except Q_0.

This leads to the discretized form of (18):

$$\mu(x,s) = g(x,s) + \frac{1}{4\pi^2} \sum_{j=1}^{N-1} \sum_{i=1}^{N-1} \int_{u_j}^{u_{j+1}} \int_{v_i}^{v_{i+1}} \frac{1}{s-k} [f(x,k_1,k_2)]_{ji} dk_1 dk_2, \tag{46}$$

where

$$g(x,s) := 1 + \frac{1}{4\pi^2} \int_S \frac{1}{s-k} [f(x,k_1,k_2)]_{ji} dk_1 dk_2, \tag{47}$$

where $S := \{[u_j, u_{j+1}] \times [v_i, v_{i+1}] \colon j \in \{0, N-1\} \text{ or } i \in \{0, N-1\}\}$, the outermost squares in the mesh. The special treatment of Q_0 is the first modification to the $\bar{\partial}$-solver introduced in [59]. Formerly, bilinear interpolation was used on all squares.

To obtain a linear system, we choose s to be the nodes of the inner mesh elements $\{s = (u_j, v_i)\}_{j,i=1}^{N}$. Then to form $g(x,s)$ and $\kappa_N \mu(x,s)$, the following integrals must be evaluated for $j, i = 0, \ldots, N$ and $s = (u_m, v_n)$, $m, n = 1, \ldots, N$:

$$J_{\alpha\beta}^{ji}(s) := \int_{u_j}^{u_{j+1}} \int_{v_i}^{v_{i+1}} \frac{k_1^\alpha k_2^\beta}{(s-k)} dk_1 dk_2, \qquad \alpha, \beta \in \{0,1\}. \tag{48}$$

The factors of k in the numerator arise from the bilinear interpolant of f. On Q_0 we must evaluate

$$\int_{T_i} \frac{k_j}{s-k} dk_1 dk_2, \qquad j = 1, 2, \quad i = 1, 2, 3, 4. \tag{49}$$

Note that when s lies on a corner of the mesh element over which we are integrating, an integrable singularity will be present in the integrand. When s does not coincide with a corner of the mesh element over which we are integrating, the above integrals are not singular, and they can be computed using a numerical quadrature method such as a 2-D Gauss–Legendre quadrature. The singular integrals in (48) and (49) can be evaluated analytically. Note that there are 16 singular integrals in (48) and 8 in (49). We omit their solutions for brevity.

Denote $\mu_{ji}(x) := \mu(x, (u_j, v_i))$. Note that $k = 0$ is not a node. Now by regrouping terms, one can write

$$\mu_{ji}(x, s) = g_{ji}(x) + \frac{1}{4\pi^2} \sum_{j=1}^{N-1} \sum_{i=1}^{N-1} A^{ji}(x) \overline{\mu_{ji}(x)}, \tag{50}$$

where $A^{ji}(x)$ is a linear combination of the $J^{ji}_{\alpha\beta}$'s and the four integrals in (49). Thus, we have the linear system

$$\mathbf{I}\mu(x) - \mathbf{A}\bar{\mu}(x) = \mathbf{g}(x), \tag{51}$$

where $\mathbf{A}(x)$ is the N^2 by N^2 matrix $\mathbf{A}(x) = (A^{ji}(x))$ and $\mathbf{I}$ is the N^2 by N^2 identity matrix. This system can be solved by equating the real and imaginary parts to obtain two linear systems in real variables with two vectors of unknowns.

Note that the factors $J^{ji}_{\alpha}(s)$ in the matrix $\mathbf{A}$ are independent of x, so they need only be computed once and stored. Then in parallel, the matrix $\mathbf{A}$ is assembled and the resulting systems (51) are solved.

To test our computed values of μ from the $\bar{\partial}$ equation, we used the Lippmann–Schwinger solver described in section 3.1 to find numerical μ for test conductivities.

The solution of the system (51) results in a set of values of $\mu(x, k)$ for $k \in M$ and some discrete set of x-values in Ω. Recall that the conductivity is given by

$$\gamma^{1/2}(x) = \lim_{k \to 0} \mu(x, k). \tag{52}$$

The value of $\mu(x, 0)$ was approximated in this implementation using bicubic interpolation on the 16 values of $\mu(x, k)$ nearest $k = 0$ in the mesh M. This is the second modification from the method described in [59].

4.2. Qualitative properties of the $\bar{\partial}$ inversion. In this section we discuss how various properties of the (approximate) scattering transform $\mathbf{t}$ are related to properties of reconstructed conductivities.

THEOREM 4.1. *Assume that $\mathbf{t}_j(k)/\bar{k} \in L^p(\mathbb{R}^2)$ for all $p \in (2-\varepsilon, 2+\varepsilon)$ for some $\varepsilon > 0$ and $j = 1, 2$. Let $\gamma_j \in C(\mathbb{R}^2)$ be given by $\bar{\partial}$ inversion from the functions $\mathbf{t}_j$ as described in Theorem 4.1 of [52]. Let $\varphi \in \mathbb{R}$, $\lambda > 0$, and $x' \in \mathbb{R}^2$; denote $z_\varphi := e^{i\varphi}(z_1 + iz_2)$ for any $z \in \mathbb{R}^2$. Then*

	$\forall k \in \mathbb{C}$		$\forall x \in \mathbb{R}^2$
(i)	$\mathbf{t}_2(k) = \mathbf{t}_1(k_{-\varphi})$	$\Rightarrow$	$\gamma_2(x) = \gamma_1(x_\varphi)$,
(ii)	$\mathbf{t}_2(k) = \mathbf{t}_1(\lambda^{-1}k)$	$\Rightarrow$	$\gamma_2(x) = \gamma_1(\lambda x)$,
(iii)	$\mathbf{t}_2(k) = \overline{\mathbf{t}_1(\bar{k})}$	$\Rightarrow$	$\gamma_2(x) = \gamma_1(-\bar{x})$,
(iv)	$\mathbf{t}_2(k) = e_k(x')\mathbf{t}_1(k)$	$\Rightarrow$	$\gamma_2(x) = \gamma_1(x - x')$.

Remark. Assume that $\gamma_j \in C^2(\mathbb{R}^2)$ have a positive lower bound and that $\gamma_j - 1$ is compactly supported for $j = 1, 2$. Further, let $\mathbf{t}_j$ be the scattering transforms corresponding to γ_j. Then equivalence holds in (i)–(iv) by Theorem 3.3 of [59].

Proof. Define ρ_φ by the operator $\rho_\varphi \mu(x, s) := \mu(x, s_\varphi)$. Define

$$\tilde{\mathbf{t}}_x(k) := \frac{1}{4\pi\bar{k}} \mathbf{t}(k) e_{-x}(k).$$

Write the integral equation (18) in operator form as

$$\mu(x, \cdot) = 1 + \bar{\partial}^{-1}(\tilde{\mathbf{t}}_x \overline{\mu(x, \cdot)}). \tag{53}$$

Since the operator $I - \bar{\partial}^{-1}(\tilde{\mathbf{t}}_x \bar{\cdot})$ is invertible [52],

$$\mu(x, \cdot) - 1 = [I - \bar{\partial}^{-1}(\tilde{\mathbf{t}}_x \bar{\cdot})]^{-1}(\bar{\partial}^{-1} \tilde{\mathbf{t}}_x). \tag{54}$$

Assume that $\mathbf{t}_2(k) = \mathbf{t}_1(k_\varphi)$. By (18) and the change of variables $z = k_\varphi$

$$\begin{aligned}
(\bar{\partial}^{-1} \tilde{\mathbf{t}}_{x_\varphi})(s) &= \frac{1}{4\pi^2} \int_{\mathbb{R}^2} \frac{\mathbf{t}_1(k)}{(s-k)\bar{k}} e_{-k}(x_\varphi) dk \\
&= \frac{1}{4\pi^2} \int_{\mathbb{R}^2} \frac{\mathbf{t}_1(k)}{(s-k)\bar{k}} e_{-k_\varphi}(x) dk \\
&= \frac{1}{4\pi^2} \int_{\mathbb{R}^2} \frac{\mathbf{t}_1(z_{-\varphi})}{(s - z_{-\varphi})\overline{z_{-\varphi}}} e_{-z}(x) dk \\
&= \frac{1}{4\pi^2} \int_{\mathbb{R}^2} \frac{\mathbf{t}_2(z)}{(s_\varphi - z)_{-\varphi}\overline{z_{-\varphi}}} e_{-z}(x) dk \\
&= \frac{1}{4\pi^2} \int_{\mathbb{R}^2} \frac{\mathbf{t}_2(z)}{(s_\varphi - z)e^{-i\varphi}\overline{z e^{-i\varphi}}} e_{-z}(x) dk \\
&= \frac{1}{4\pi^2} \int_{\mathbb{R}^2} \frac{\mathbf{t}_2(z)}{(s_\varphi - z)\bar{z}} e_{-z}(x) dk \\
&= (\bar{\partial}^{-1} \tilde{\mathbf{t}}_x)(s_\varphi) \\
&= \rho_\varphi (\bar{\partial}^{-1} \tilde{\mathbf{t}}_x)(s).
\end{aligned}$$

Thus, $\bar{\partial}^{-1}(\tilde{\mathbf{t}}_{x_\varphi} \overline{\mu(x_\varphi, \cdot)})(s) = \rho_\varphi(\bar{\partial}^{-1} \tilde{\mathbf{t}}_{x} \bar{\cdot}) \rho_{-\varphi} \overline{\mu(x_\varphi, s)}$. Therefore,

$$\begin{aligned}
\mu_1(x_\varphi, s) &= 1 + [I - \bar{\partial}^{-1}(\tilde{\mathbf{t}}_{x_\varphi} \bar{\cdot})]^{-1}(\bar{\partial}^{-1} \tilde{\mathbf{t}}_{x_\varphi})(s) \\
&= 1 + \rho_\varphi [I - \bar{\partial}^{-1}(\tilde{\mathbf{t}}_x \bar{\cdot})]^{-1} \rho_{-\varphi} \rho_\varphi (\bar{\partial}^{-1} \tilde{\mathbf{t}}_x)(s) \\
&= 1 + \rho_\varphi [I - \bar{\partial}^{-1}(\tilde{\mathbf{t}}_x \bar{\cdot})]^{-1}(\bar{\partial}^{-1} \tilde{\mathbf{t}}_x)(s) \\
&= \mu_2(x, s_\varphi).
\end{aligned}$$

Taking the limit as $s \to 0$, by (19) we have that $\gamma_2(x) = \gamma_1(x_\varphi)$. The cases (ii), (iii), and (iv) can be proved similarly to case (i). ∎

4.3. Reconstruction from truncated scattering transform. Let γ be a C^4 conductivity and $\mathbf{t}$ its scattering transform. We present a new result: The conductivities γ_R reconstructed from $\mathbf{t}$ truncated at $|k| = R$ converge pointwise to γ when $R \to \infty$.

For any radius $R > 0$, define a function $\mathbf{t}_R : \mathbb{C} \to \mathbb{C}$ by

$$\mathbf{t}_R(k) := \chi_R(k) \mathbf{t}(k), \qquad \chi_R := \chi_{\{|k| < R\}}. \tag{55}$$

Since $\mathbf{t}$ satisfies the assumptions of Theorem 4.1 in [52], so will $\mathbf{t}_R$. Let

$$\mathbf{t}_{\mathbf{x}}^{\infty}(k) := \frac{1}{4\pi\bar{k}}\mathbf{t}(k)e_{-x}(k) \quad \text{and} \quad \mathbf{t}_{\mathbf{x}}^{\mathbf{R}}(k) := \frac{1}{4\pi\bar{k}}\mathbf{t}_R(k)e_{-x}(k); \tag{56}$$

then the solutions of the following integral equations exist:

$$\mu(x,\cdot) = 1 + \partial_{\bar{k}}^{-1}(\mathbf{t}_{\mathbf{x}}^{\infty}\overline{\mu(x,\cdot)}) \quad \text{and} \quad \mu_R(x,\cdot) = 1 + \partial_{\bar{k}}^{-1}(\mathbf{t}_{\mathbf{x}}^{\mathbf{R}}\overline{\mu_R(x,\cdot)}). \tag{57}$$

We have $\gamma^{1/2}(x) = \lim_{k\to 0}\mu(x,k)$. Define γ_R by

$$\gamma_R^{1/2}(x) := \lim_{k\to 0}\mu_R(x,k).$$

This γ_R is thought of as an approximation to the actual conductivity. By [52] we know that γ_R is Hölder continuous, bounded away from zero, and asymptotically equal to 1 when $|x|$ grows.

THEOREM 4.2. *Let $\Omega \subset \mathbb{R}^2$ be the unit disc and $\gamma \in C^{2+m}(\Omega)$ with $m > 1$. Assume that $\gamma \equiv 1$ near $\partial\Omega$ and $0 < c \le \gamma(x)$ for all $x \in \Omega$. Let $\mathbf{t}$ be the corresponding scattering transform defined by (10), and define $\mathbf{t}_R$, μ_R, and γ_R as above for any $R > 0$. Then the following estimate holds for large R:*

$$\|\sqrt{\gamma} - \sqrt{\gamma_R}\|_{L^\infty(\Omega)} \le CR^{-m+1}. \tag{58}$$

For the proof of the theorem, we need a result analogous to Lemma 2.2.1 [47].

LEMMA 4.3. *Assume $1/M \le \gamma(x)$ and $\|\gamma\|_{W^{2,p}(\Omega)} \le M$ for some $M < \infty$ and $1 < p < 2$. Then*

$$\sup_{x\in\Omega}\|\mu(x,\cdot) - \mu_R(x,\cdot)\|_{L^r(\mathbb{C})} \le C_M \left\| \frac{\mathbf{t}(k) - \mathbf{t}_R(k)}{\bar{k}} \right\|_{L^{\frac{2r}{r+2}}} \tag{59}$$

with C_M independent of x and k; here $r > p'$ with $1/p + 1/p' = 1$.

Proof. Define operators A and A_R by

$$Af := \partial_{\bar{k}}^{-1}(\mathbf{t}_{\mathbf{x}}^{\infty}\bar{f}), \qquad A_R f := \partial_{\bar{k}}^{-1}(\mathbf{t}_{\mathbf{x}}^{\mathbf{R}}\bar{f}).$$

Compute

$$\begin{aligned} \mu(x,\cdot) - \mu_R(x,\cdot) &= \partial_{\bar{k}}^{-1}(\mathbf{t}_{\mathbf{x}}^{\infty}\overline{\mu(x,\cdot)}) - \partial_{\bar{k}}^{-1}(\mathbf{t}_{\mathbf{x}}^{\mathbf{R}}\overline{\mu_R(x,\cdot)}) \\ &= \partial_{\bar{k}}^{-1}(\mathbf{t}_{\mathbf{x}}^{\infty} - \mathbf{t}_{\mathbf{x}}^{\mathbf{R}})\overline{\mu(x,\cdot)} - \partial_{\bar{k}}^{-1}\mathbf{t}_{\mathbf{x}}^{\mathbf{R}}(\overline{\mu_R(x,\cdot)} - \overline{\mu(x,\cdot)}), \end{aligned} \tag{60}$$

or, by the definition of A_R,

$$(I - A_R)(\mu(x,k) - \mu_R(x,k)) = \partial_{\bar{k}}^{-1}(\mathbf{t}_{\mathbf{x}}^{\infty} - \mathbf{t}_{\mathbf{x}}^{\mathbf{R}})\overline{\mu(x,k)}. \tag{61}$$

From the proof of Theorem 4.1 in [52] we know that $I - A$ is invertible on L^r. Moreover, the proof of Lemma 2.2.1 in [47] shows that

$$\|(I - A)^{-1}\|_{L(L^r)} \le C'_M$$

with C'_M independent of x and k. We show that $A_R \to A$ in the topology of $L(L^r)$ when $R \to \infty$. We have $\|A - A_R\|_{L(L^r)} = \|(A - A_R)^*\|_{L(L^{r'})}$ for the adjoint operator. Consider inequality (4.6) of [52]:

$$\|(A - A_R)^* f\|_{L^{r'}} = \|(\mathbf{t}_{\mathbf{x}}^{\infty} - \mathbf{t}_{\mathbf{x}}^{\mathbf{R}})\partial^{-1} f\|_{L^{r'}} \le C\|\mathbf{t}_{\mathbf{x}}^{\infty} - \mathbf{t}_{\mathbf{x}}^{\mathbf{R}}\|_{L^2}\|f\|_{L^{r'}},$$

and note that

$$\|\mathbf{t}_{\mathbf{x}}^{\infty} - \mathbf{t}_{\mathbf{x}}^{\mathbf{R}}\|_{L^2}^2 = \frac{1}{4\pi} \int_{|k|>R} \left| \frac{\mathbf{t}(k)}{\bar{k}} \right|^2 dk_1 dk_2.$$

By Theorem 3.2 of [59] we can choose R so large that

$$|\mathbf{t}(k)| \leq C_1 |k|^{-m} \tag{62}$$

for $|k| > R$, so for such R we have

$$\|\mathbf{t}_{\mathbf{x}}^{\infty} - \mathbf{t}_{\mathbf{x}}^{\mathbf{R}}\|_{L^2} \leq C \left(\int_R^{\infty} \rho^{-2m-1} d\rho \right)^{1/2} = CR^{-m} \to 0 \text{ when } R \to \infty.$$

We have established $\|A - A_R\|_{L(L^r)} \to 0$ when $R \to \infty$. Since the set of invertible operators in $L(L^r)$ is open, the operator $I - A_R$ will be invertible for all large enough R and satisfy

$$\|(I - A_R)^{-1}\|_{L(L^r)} \leq \|(I - A)^{-1}\|_{L(L^r)} + 1 \leq C_M. \tag{63}$$

By (63), Lemma 1.2 of [52], and (61) we have for fixed $x \in \Omega$

$$\begin{aligned} \|\mu(x,\cdot) - \mu_R(x,\cdot)\|_{L^r} &\leq \|(I - A_R)^{-1}\|_{L(L^r)} \|\partial_{\bar{k}}^{-1}(\mathbf{t}_{\mathbf{x}}^{\infty} - \mathbf{t}_{\mathbf{x}}^{\mathbf{R}}) \overline{\mu(x,\cdot)}\|_{L^r} \\ &\leq C_M \|(\mathbf{t}_{\mathbf{x}}^{\infty} - \mathbf{t}_{\mathbf{x}}^{\mathbf{R}}) \overline{\mu(x,\cdot)}\|_{L^{\frac{2r}{r+2}}}. \end{aligned}$$

Since $\sup_x \|\mu(x,\cdot)\|_{L^\infty} < \infty$ by Theorem 4.1 in [52] and $|e_{-x}(k)| = 1$, the lemma is proved. □

Proof of Theorem 4.2. For fixed $x \in \Omega$

$$\sqrt{\gamma(x)} - \sqrt{\gamma_R(x)} = \lim_{k \to 0} (\mu(x,k) - \mu_R(x,k)) \tag{64}$$

and from (60)

$$\begin{aligned} \mu(x,\cdot) - \mu_R(x,\cdot) &= \partial_{\bar{k}}^{-1}(\mathbf{t}_{\mathbf{x}}^{\infty} - \mathbf{t}_{\mathbf{x}}^{\mathbf{R}})1 + \partial_{\bar{k}}^{-1}(\mathbf{t}_{\mathbf{x}}^{\infty} - \mathbf{t}_{\mathbf{x}}^{\mathbf{R}})(\overline{\mu(x,\cdot)} - 1) \\ &\quad - \partial_{\bar{k}}^{-1} \mathbf{t}_{\mathbf{x}}^{\mathbf{R}} (\overline{\mu_R(x,\cdot)} - \overline{\mu(x,\cdot)}). \end{aligned} \tag{65}$$

We will bound each of the three terms in the right-hand side of (65).

Consider the first term in the right-hand side of (65). Recall that

$$\partial_{\bar{k}}^{-1} f(z) = \frac{1}{\pi} \int_{\mathbb{R}^2} \frac{f(w)}{z - w} dw_1 dw_2, \tag{66}$$

where $w = w_1 + iw_2$ and $z = z_1 + iz_2$. Note that $|e_{-x}(k)| = 1$. So by (62)

$$\begin{aligned} \lim_{k \to 0} |(\partial_{\bar{k}}^{-1}(\mathbf{t}_{\mathbf{x}}^{\infty} - \mathbf{t}_{\mathbf{x}}^{\mathbf{R}})1)(k)| &\leq \frac{1}{4\pi^2} \int_{\mathbb{R}^2} \frac{|(\mathbf{t}(w) - \mathbf{t}_R(w)) e_{-x}(w)|}{|\bar{w} w|} dw_1 dw_2 \\ &\leq \frac{1}{4\pi^2} \int_{|w|>R} \frac{C_1}{|w|^{2+m}} dw_1 dw_2 = \tilde{C} R^{-m}. \end{aligned}$$

Consider the second term in the right-hand side of (65). By Theorem 4.1 of [52] there exists such a constant $C_2 > 0$ that

$$\sup_{x,k} |\overline{\mu(x,k)} - 1| < C_2. \tag{67}$$

Hence by (67) and (62)

$$\begin{aligned}
&\lim_{k\to 0} |\partial_{\bar{k}}^{-1}(\mathbf{t}_{\mathbf{x}}^{\infty} - \mathbf{t}_{\mathbf{x}}^{\mathbf{R}})(\overline{\mu(x,\cdot)} - 1)(k)| \\
&= \left| \frac{1}{4\pi^2} \int_{\mathbb{R}^2} \frac{(\mathbf{t}(w) - \mathbf{t}_R(w)) e_{-x}(w) (\overline{\mu(x,w)} - 1)}{\bar{w}w} dw_1 dw_2 \right| \\
&\leq \frac{C_2}{4\pi^2} \int_{\mathbb{R}^2} \frac{|\mathbf{t}(w) - \mathbf{t}_R(w)||e_{-x}(w)|}{|w|^2} dw_1 dw_2 \\
&\leq \frac{C_2}{4\pi^2} \int_{|w|>R} \frac{\mathbf{t}(w)}{|w|^2} dw_1 dw_2 \leq C_3 R^{-m}.
\end{aligned}$$

Consider the third term in the right-hand side of (65). By Hölder's inequality and Lemma 4.3

$$\begin{aligned}
&\lim_{k\to 0} |\partial_{\bar{k}}^{-1} \mathbf{t}_{\mathbf{x}}^{\mathbf{R}} (\overline{\mu_R(x,\cdot)} - \overline{\mu(x,\cdot)})(k)| \\
&= \left| \frac{1}{4\pi^2} \int_{\mathbb{R}^2} \frac{\mathbf{t}_R(w) e_{-x}(w) (\overline{\mu_R(x,w)} - \overline{\mu(x,w)})}{\bar{w}w} dw_1 dw_2 \right| \\
&\leq \frac{1}{4\pi^2} \|\overline{\mu_R(x,\cdot)} - \overline{\mu(x,\cdot)}\|_{L^r} \left\| \frac{\mathbf{t}_R(w)}{|w|^2} \right\|_{L^{r'}} \\
&\leq \frac{C_M}{4\pi^2} \left\| \frac{\mathbf{t}(w) - \mathbf{t}_R(w)}{\bar{w}} \right\|_{L^{\frac{2r}{r+2}}} \left\| \frac{\mathbf{t}_R(w)}{|w|^2} \right\|_{L^{r'}} \\
&= \frac{C_M}{4\pi^2} \left(\int_{|w|>R} \left(\frac{|\mathbf{t}(w)|}{|\bar{w}|} \right)^{\frac{2r}{r+2}} dw_1 dw_2 \right)^{\frac{r+2}{2r}} \left(\int_{|w|<R} \left(\frac{|\mathbf{t}(w)|}{|w|^2} \right)^{r'} dw_1 dw_2 \right)^{1/r'},
\end{aligned}$$

where $1/r + 1/r' = 1$. Again by (62)

$$\begin{aligned}
\int_{|w|>R} \left(\frac{|\mathbf{t}(w)|}{|\bar{w}|} \right)^{\frac{2r}{r+2}} dw_1 dw_2 &\leq \int_{|w|>R} \left(\frac{C_1}{|w|^{m+1}} \right)^{\frac{2r}{r+2}} dw_1 dw_2 \\
&= 2\pi C_1 \int_R^{\infty} \rho^{\frac{-2(m+1)r}{r+2}} \rho d\rho \\
&= C_4 R^{\frac{-2(m+1)r}{r+2}+2}.
\end{aligned}$$

By Theorem 3.1 of [59] (see also [60]) we can choose $0 < \epsilon < R$ sufficiently small so that for $|w| < \epsilon$

$$|\mathbf{t}(w)| \leq C_\epsilon |w|^2. \tag{68}$$

Then

$$\begin{aligned}
\int_{|w|<R} \left(\frac{|\mathbf{t}(w)|}{|w|^2} \right)^{r'} dw_1 dw_2 &= \int_{|w|<\epsilon} \left(\frac{|\mathbf{t}(w)|}{|w|^2} \right)^{r'} dw_1 dw_2 + \int_{\epsilon<|w|<R} \left(\frac{|\mathbf{t}(w)|}{|w|^2} \right)^{r'} dw_1 dw_2 \\
&\leq \int_{|w|<\epsilon} C_\epsilon^{r'} dw_1 dw_2 + \int_{\epsilon<|w|<R} \frac{C_5^{r'}}{|w|^{2r'}} dw_1 dw_2 \\
&= \tilde{C}_\epsilon (1 + R^{-2r'+2}).
\end{aligned}$$

TABLE 1
Some features of the example conductivities. Note the division of examples to three groups.

	Smoothness	Min$\gamma(x)$	Max$\gamma(x)$	Radial?	Accurate Λ_γ?	Accurate $\mathbf{t}^{\exp}$?
γ_1	4	1	2.2	$\surd$	$\surd$	$\surd$
γ_2	4	0.6	4	$\surd$	$\surd$	$\surd$
γ_3	∞	1	4	$\surd$	$\surd$	$\surd$
γ_4	4	0.15	4	–	–	–
γ_5	∞	1	4	–	–	$\surd$
γ_6	4	0.6	4	–	–	$\surd$
γ_7	4	1	2.2	–	–	$\surd$

Since $2 < r < \infty$ we have $1 < r' < 2$ and, using (64),

$$\begin{aligned}|\sqrt{\gamma(x)} - \sqrt{\gamma_R(x)}| &= \lim_{k\to 0} |\partial_{\bar{k}}^{-1} \mathbf{t}_{\mathbf{x}}^{\mathbf{R}}(\overline{\mu_R(x,\cdot)} - \overline{\mu(x,\cdot)})(k)| \\ &\le C_6 R^{(\frac{-2(m+1)r}{r+2}+2)(\frac{r+2}{2r})}(1 + R^{-2r'+2})^{1/r'} \\ &= C_6 R^{-m+\frac{2}{r}}(1 + R^{-2r'+2})^{1/r'} \le C R^{-m+1}. \qquad \square\end{aligned}$$

5. Numerical examples. We present seven examples divided into three groups. The example conductivities have varying degrees of smoothness and different qualitative features such as dips or hills near the boundary.

The first group of examples, presented in section 5.1, consists of radial conductivities γ_1, γ_2, and γ_3. Of these, we have already treated γ_3 in [59] and γ_2 in [61] with nonnoisy boundary data. We show here new reconstructions of these radial conductivities from noisy and nonnoisy boundary data by implementing both steps of Nachman's method. We demonstrate the differences of the reconstructions done with $\mathbf{t}^{\mathrm{LS}}$, $\mathbf{t}^{\mathrm{B}}$, $\tilde{\mathbf{t}}^{\mathrm{B}}$, $\mathbf{t}^{\exp}$, and $\tilde{\mathbf{t}}^{\exp}$. We also study the nature of the pointwise convergence proved in Theorem 4.2 by reconstructing from truncated (exact) scattering transform.

The second group of examples presented in section 5.2 contains one nonsymmetric conductivity γ_4. We study the pointwise convergence of reconstructions from truncated $\mathbf{t}_4^{\mathrm{LS}}$ with growing cutoff radius.

The third group of examples is presented in section 5.3 and consists of nonradial conductivities γ_5, γ_6, and γ_7 obtained by composing the radial conductivities γ_3, γ_2, and γ_1, respectively, with a conformal map. For these conductivities it is possible to compute $\mathbf{t}^{\exp}$ with good accuracy, and we are able to compare reconstructions of these conductivities from good-quality $\mathbf{t}^{\mathrm{LS}}$ and $\mathbf{t}^{\exp}$.

We summarize properties of the examples we treat in this paper in Table 1. For plots of all the example conductivities, see Figure 2. We present all numerical parameters and computational details for Example 1. Unless otherwise stated, the parameters are the same for Examples 2–7.

5.1. First group: Radially symmetric conductivities $\gamma_1, \gamma_2, \gamma_3$. From symmetry Theorem 3.3 of [59] and Lemmas 3.2 and 3.3 of this paper, we know that $\mathbf{t}_i, \mathbf{t}_i^{\mathrm{B}}$, and $\mathbf{t}_i^{\exp}$ are radial and real-valued for $i = 1, 2, 3$. Thus it is enough to compute them for real and positive k only.

We list in Table 2 some approximate eigenvalue differences $\lambda_n - n$ corresponding to Dirichlet-to-Neumann maps $\Lambda_{\gamma_1}, \Lambda_{\gamma_2}, \Lambda_{\gamma_3}$.

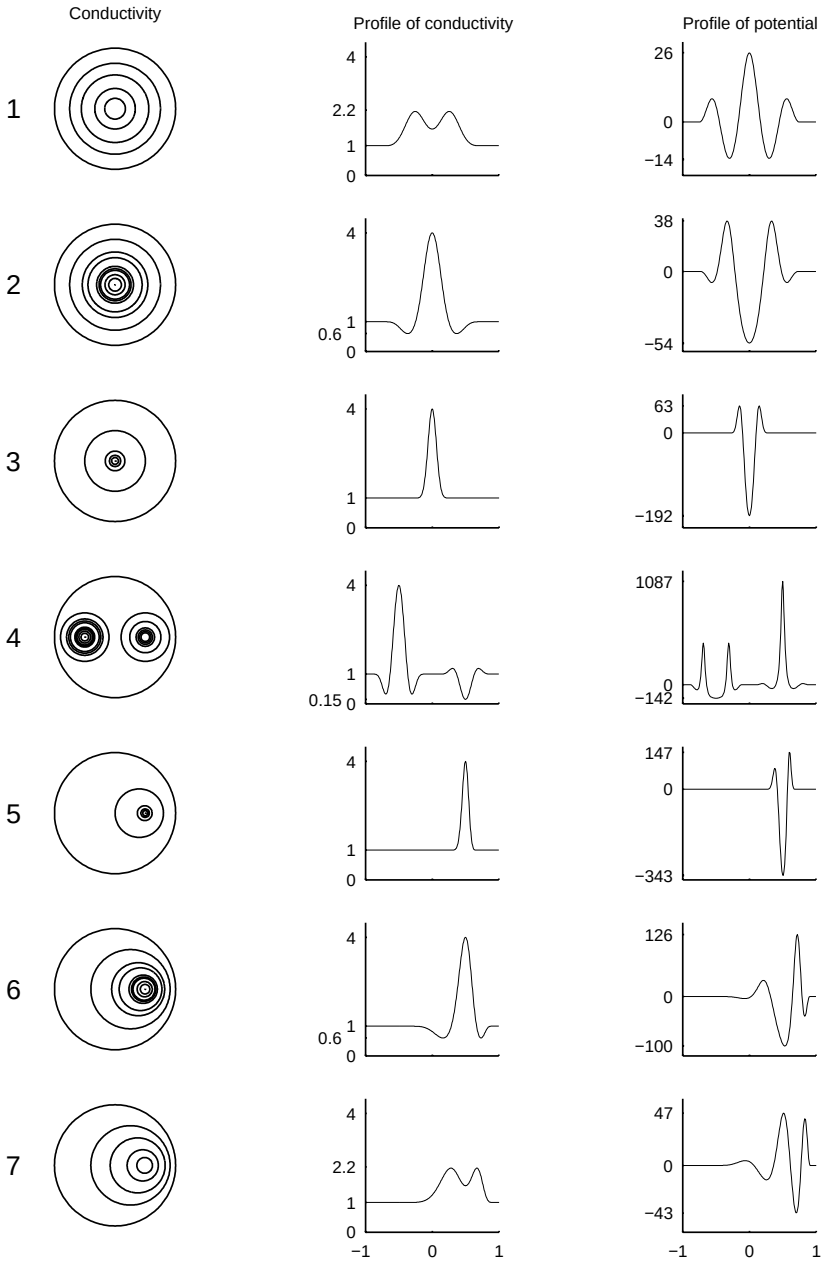

FIG. 2. *Plots of all seven examples we treat in this paper. Left column shows contour plots in unit disc of each conductivity. Center column shows the restriction of conductivity to the* x_1 *axis. For radially symmetric Examples* 1–3 *this profile completely determines the conductivity. Right column shows the restriction of potential to the* x_1 *axis. Again, for radially symmetric examples Examples* 1–3 *this profile completely determines the potential. Note that conductivities* γ_5, γ_6, *and* γ_7 *are distorted versions of* γ_3, γ_2, *and* γ_1, *respectively.*

TABLE 2

Approximate eigenvalue differences $\lambda_n - n$ for the radial Examples 1, 2, and 3. Here n is the nth eigenvalue of the Dirichlet-to-Neumann map Λ_1 corresponding to the homogeneous conductivity 1, and we denote by λ_n the nth eigenvalue of the Dirichlet-to-Neumann map $\Lambda_{\gamma_1}, \Lambda_{\gamma_2}$, or Λ_{γ_3}. Each approximate difference $\lambda_n - n$ has two significant digits even though the digits appear at very different orders of magnitude; this is due to the fact that our algorithm computes the difference directly. The exponential decay of the difference $\lambda_n - n$ demonstrates that with finite-precision EIT measurements we can determine only the few first eigenvalues.

n	Example 1 $\lambda_n - n$	Example 2 $\lambda_n - n$	Example 3 $\lambda_n - n$
1	0.16	−0.045	0.015
2	0.078	−0.052	0.00054
3	0.032	−0.025	0.000020
4	0.012	−0.010	0.00000076
5	0.0050	−0.0040	0.000000032
6	0.0020	−0.0016	0.0000000014
7	0.00085	−0.00064	0.000000000069
8	0.00036	−0.00026	0.0000000000035
9	0.00016	−0.00011	0.00000000000019
10	0.000069	−0.000046	0.000000000000010
11	0.000031	−0.000020	0.00000000000000059
12	0.000014	−0.0000088	0.00000000000000035
13	0.0000065	−0.0000039	0.0000000000000000022
14	0.0000030	−0.0000018	0.0000000000000000014
15	0.0000014	−0.00000080	0.00000000000000000000088
16	0.00000068	−0.00000037	0.00000000000000000000058

Define a radially symmetric conductivity $\gamma \in C^m(\mathbb{R}^2)$ by

$$\gamma(x) := (\alpha F_\rho(|x|) + 1)^2, \tag{69}$$

where F_ρ is a $C_0^m(\mathbb{R})$, $m \geq 2$, function satisfying $F_\rho(t) = F_\rho(-t)$ and having support in the interval $[-\rho, \rho]$. Moreover, $\alpha \in \mathbb{R}$ is such a constant that $\alpha F_\rho(|x|) > -1$ for all $x \in \mathbb{R}^2$. The Schrödinger potential q corresponding to γ is the $C_0^{m-2}(\mathbb{R}^2)$ function given outside the origin by

$$q(x) := \frac{\Delta \gamma^{1/2}(x)}{\gamma^{1/2}(x)} = \frac{\Delta F_\rho(|x|)}{F_\rho(|x|) + 1/\alpha}. \tag{70}$$

Note that we always have $\gamma \equiv 1$ and $q \equiv 0$ for $|x| \geq \rho$. We present three radial conductivities for our numerical examples with different choices of F_ρ and α.

Example 1. Define $F_\rho \in C_0^4(\mathbb{R})$ for $-\rho \leq x \leq \rho$ by

$$F_\rho(x) := (x^2 - \rho^2)^4 \left(1.5 - \cos \frac{3\pi x}{2\rho}\right), \tag{71}$$

and $F_\rho(x) = 0$ for $|x| > \rho$. We define γ_1 by formula (69) with $\alpha = 5$ and $\rho = 3/4$. Then $\max |\gamma_1(x)| \approx 2.2$. Plots of γ_1 and the corresponding potential q_1 are found in Figure 2.

The exact scattering transform $\mathbf{t}_1^{\text{LS}}(k)$ was computed in the interval $k \in [.01, 30] \subset \mathbb{R}_+$ as described in section 3.1. The computation was carried out using Matlab and an IBM personal computer with a 733 MHz Pentium III processor. We chose $M = 512$ in the interval $I_1 := [.01, 1[$, $M = 256$ in the interval $I_2 := [1, 5[$, and $M = 128$ in the

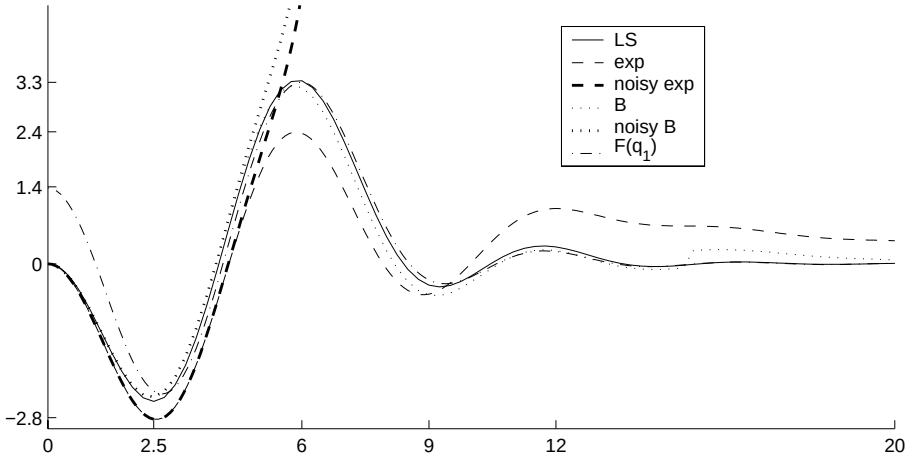

FIG. 3. *Profiles of the following radial and real-valued functions: scattering transform* $\mathbf{t}_1^{\mathrm{LS}}$ (*solid line*), *approximate scattering transforms* $\mathbf{t}_1^{\mathrm{B}}$ (*thin dotted line*) *and* $\mathbf{t}_1^{\exp}$ (*thin dashed line*), *and the Fourier transform* $\hat{q}_1(2|k|)$ (*dot-dash line*). *Also, plots of real parts of* $\tilde{\mathbf{t}}_1^{\mathrm{B}}(k)$ (*thick dotted line*) *and* $\tilde{\mathbf{t}}_1^{\exp}(k)$ (*thick dashed line*) *along positive* k_1 *axis.*

interval $I_3 := [5, 30[$. Computation time for one value of $\mathbf{t}_1^{\mathrm{LS}}$ was 10 minutes in I_1, 30 seconds in I_2, and 6 seconds in I_3. Some 70% of the time was spent evaluating the fundamental solution g_k. See Figure 3 for a plot of $\mathbf{t}_1^{\mathrm{LS}}$.

Eigenvalues of Λ_{γ_1} were computed for $n = 1, \ldots, 75$ with the method described in [59]. See Table 2 for few first eigenvalues.

We verified our computational scheme for $\mathbf{t}_1^{\mathrm{LS}}$ by comparing it to the numerical scattering transform $\mathbf{t}_1'$ achieved by solving (15) numerically using exact data without regularization. The relative difference $|\mathbf{t}_1^{\mathrm{LS}}(k) - \mathbf{t}_1'(k)| / \max|\mathbf{t}_1^{\mathrm{LS}}(k)|$ between these computations was seen to be less than 0.003 in the range $k \in [0.01, 15]$. For $k > 15$ the computation of $\mathbf{t}_1'$ becomes inaccurate due to the finite number of eigenvalues used to represent Λ_γ. Since these two methods of computation are completely different and the computation of $\mathbf{t}_1^{\mathrm{LS}}$ gets easier when $|k|$ grows, we have a reason to believe that $\mathbf{t}_1^{\mathrm{LS}}$ has good accuracy.

The approximate scattering transform $\mathbf{t}_1^{\exp}$ was computed from the series (41) truncated to $n \leq 75$ for $k \in [0, 20]$. We repeated the computation with $n \leq 55$; the results agreed to machine precision. The regularized scattering transform $\mathbf{t}_1^{\mathrm{B}}$ was computed as described in section 3.3 with trigonometric approximation of order 64 for $k \in [0, 20]$. We repeated the computation with order 32; the relative error between the two computations was seen to be less than 10^{-5} in the interval $[0, 15]$. Profiles of $\mathbf{t}_1^{\exp}$ and $\mathbf{t}_1^{\mathrm{B}}$ are found in Figure 3.

Noisy EIT measurements on electrodes were simulated as described in section 3.2, and we obtained a matrix representation of Λ_{γ_1} from which $\tilde{\mathbf{t}}_1^{\mathrm{B}}$ and $\tilde{\mathbf{t}}_1^{\exp}$ were computed as above. Note that $\tilde{\mathbf{t}}_1^{\mathrm{B}}$ and $\tilde{\mathbf{t}}_1^{\exp}$ are complex-valued. Plots of $\Re(\tilde{\mathbf{t}}_1^{\mathrm{B}})$ and $\Re(\tilde{\mathbf{t}}_1^{\exp})$ along the positive k_1 axis are found in Figure 3. Note from Figure 3 that the noisy approximations blow up as $|k| \to \infty$. For that reason, they were truncated in the reconstructions using the $\bar{\partial}$ equation. In practice, $\tilde{\mathbf{t}}_1^{\mathrm{B}}$ was set to zero for $|k| > 6$, giving a maximum value of $\Re(\tilde{\mathbf{t}}_1^{\mathrm{B}})$ of approximately 5.7, and $\tilde{\mathbf{t}}_1^{\exp}$ was set to zero for $|k| > 6.1$, giving a maximum value of $\Re(\tilde{\mathbf{t}}_1^{\exp})$ of approximately 5.4.

The conductivity γ_1 was reconstructed from each scattering transform using the

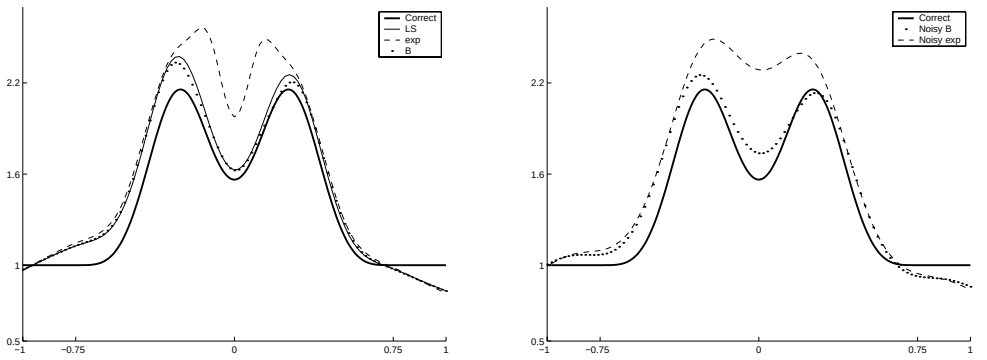

FIG. 4. *Profiles of the reconstructed conductivities for Example* 1. *The actual* γ_1 *is the thick solid line. The other plots denote reconstructions from* $\mathbf{t}_1^{LS}$ *(thin line),* $\mathbf{t}_1^{\exp}$, $\mathbf{t}_1^{B}$, $\tilde{\mathbf{t}}_1^{B}$, *and* $\tilde{\mathbf{t}}_1^{\exp}$.

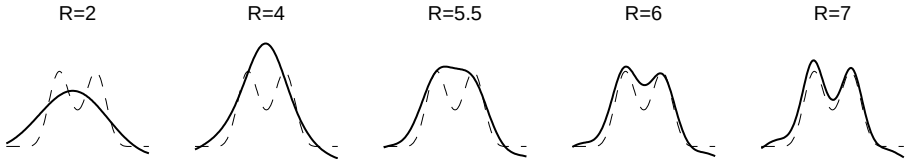

FIG. 5. *Profiles of reconstructions from truncated* $\mathbf{t}_1^{LS}$. *The actual* γ_1 *is the dashed line. The reconstruction is the solid line.*

numerical solver for the $\bar{\partial}$ equation described in section 4 using the uniform k-mesh $[-20, 20]^2$ with $h \approx 1$. For each x-value, the value of $\gamma_1^{1/2}(x)$ was obtained by using bicubic interpolation on the 16 values of $\Re(\mu_1(x,k))$ nearest $k = 0$. The computations were performed in Fortran 90 on the Cray T90 at the San Diego Supercomputer Center. The average computation time for computing $\mu_1(x,k)$ on the above mesh for one x-value was 4 seconds, with the majority of the time spent solving the linear system.

Plots of the approximate conductivities reconstructed from $\mathbf{t}_1^{\mathrm{LS}}$, $\mathbf{t}_1^{\mathrm{B}}$, $\tilde{\mathbf{t}}_1^{\mathrm{B}}$, $\mathbf{t}_1^{\exp}$, and $\tilde{\mathbf{t}}_1^{\exp}$ are found in Figure 4. Reconstructions were computed along the real axis for the x-values $(-1,0), (-.98,0), \ldots, (.98,0), (1,0)$.

To study reconstructions from truncated scattering transforms, $\mathbf{t}_1^{\mathrm{LS}}(k)$ was set to 0 for values of $|k| > R$ for a sequence of R values. In Figure 5 we include plots of reconstructions from truncated $\mathbf{t}_1^{\mathrm{LS}}$ with $R = 7, 6, 5.5, 4, 2$. From these plots it is evident that significant information about γ_1 is found in $\mathbf{t}_1(k)$ for small values of k since the reconstructions do not lose significant qualitative information about γ_1 until $R < 6$. These results are very encouraging since noise in the measurement data leads to truncated approximations to the scattering transform (see, for example, the plots of $\tilde{\mathbf{t}}_1^{\mathrm{B}}$ and $\tilde{\mathbf{t}}_1^{\exp}$ in Figure 3).

Example 2. Define $F_\rho \in C_0^4(\mathbb{R})$ for $-\rho \le x \le \rho$ by

$$F_\rho(x) := (x^2 - \rho^2)^4 \cos \frac{3\pi x}{2\rho}, \tag{72}$$

and $F_\rho(x) = 0$ for $|x| > \rho$. We define γ_2 by formula (69) with $\alpha = 10$ and $\rho = 3/4$. Then $\max|\gamma_2(x)| \approx 4$. Plots of γ_2 and the corresponding potential q_2 are found in Figure 2.

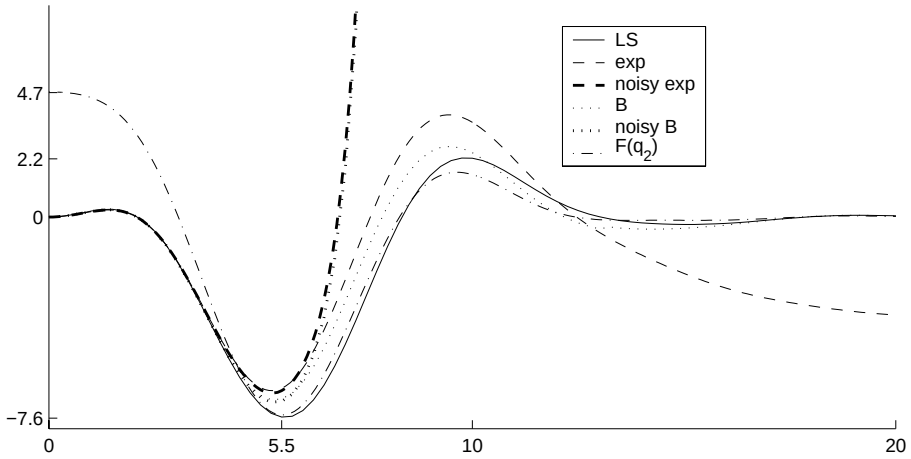

FIG. 6. *Profiles of the following radial and real-valued functions: scattering transform* $\mathbf{t}_2^{\mathrm{LS}}$ (*solid line*), *approximate scattering transforms* $\mathbf{t}_2^{\mathrm{B}}$ (*thin dotted line*) *and* $\mathbf{t}_2^{\mathrm{exp}}$ (*thin dashed line*), *and the Fourier transform* $\hat{q}_2(2|k|)$ (*dot-dash line*). *Also, plots of real parts of* $\tilde{\mathbf{t}}_2^{\mathrm{B}}(k)$ (*thick dotted line*) *and* $\tilde{\mathbf{t}}_2^{\mathrm{exp}}(k)$ (*thick dashed line*) *along positive* k_1 *axis.*

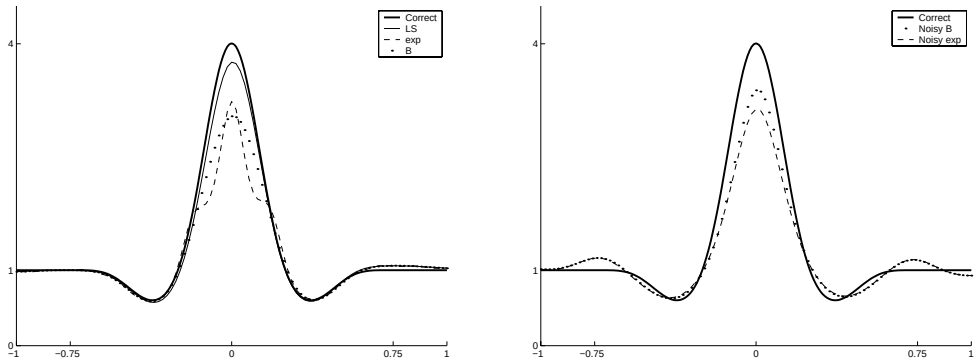

FIG. 7. *Profiles of the reconstructed conductivities for Example* 2. *The actual* γ_2 *is the thick solid line. The other plots denote reconstructions from* $\mathbf{t}_2^{LS}$, $\mathbf{t}_2^{\mathrm{exp}}$, $\mathbf{t}_2^{B}$, $\tilde{\mathbf{t}}_2^{B}$, *and* $\tilde{\mathbf{t}}_2^{\mathrm{exp}}$.

The functions $\mathbf{t}_2^{\mathrm{LS}}$, $\mathbf{t}_2^{\mathrm{B}}$, $\mathbf{t}_2^{\mathrm{exp}}$, $\tilde{\mathbf{t}}_2^{\mathrm{B}}$, and $\tilde{\mathbf{t}}_2^{\mathrm{exp}}$ were computed similarly to Example 1. See Figure 6 for a plot. Note that except for small $|k|$ values, the function $\mathbf{t}_2^{\mathrm{LS}}(|k|)$ is very similar to $\hat{q}_2(2|k|)$.

This example was considered in [61] where reconstructions of γ_2 from $\mathbf{t}_2^{\mathrm{exp}}$ and $\mathbf{t}_2^{\mathrm{LS}}$ were given. Here we include the reconstructions from $\mathbf{t}_2^{\mathrm{LS}}$, $\mathbf{t}_2^{\mathrm{B}}$, $\tilde{\mathbf{t}}_2^{\mathrm{B}}$, $\mathbf{t}_2^{\mathrm{exp}}$, and $\tilde{\mathbf{t}}_2^{\mathrm{exp}}$ in Figure 7. In this example $\tilde{\mathbf{t}}_2^{\mathrm{B}}$ was set to zero for $|k| > 7.2$, and $\tilde{\mathbf{t}}_2^{\mathrm{exp}}$ was set to zero for $|k| > 7.25$.

Reconstructions of γ_2 from the truncated $\mathbf{t}_2^{\mathrm{LS}}$ with $R = 7, 6.5, 6, 5, 4$ are plotted in Figure 8. Note that significant qualitative information is retained about the conductivity until $R < 5$.

Example 3. Fix $0 < \rho < 1$ and let $F_\rho \in C_0^\infty(\mathbb{R})$ for $-\rho \le x \le \rho$ be given by

$$F_\rho(x) := e^{-\frac{2(\rho^2+x^2)}{(x+\rho)^2(x-\rho)^2}}, \tag{73}$$

and $F_\rho(x) = 0$ for $|x| > \rho$. We define γ_3 by formula (69) with $\alpha = e^8$ and $\rho = 1/2$.

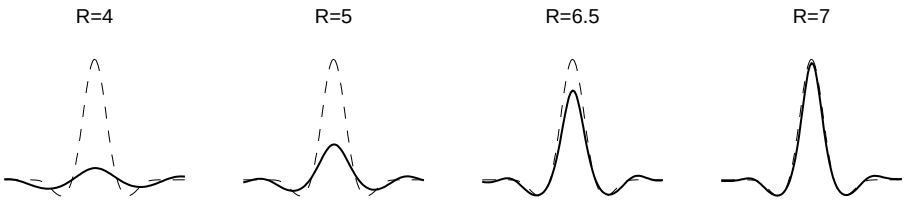

FIG. 8. *Profiles of reconstructions from truncated* $\mathbf{t}_2^{LS}$. *The actual* γ_2 *is the dashed line. The reconstruction is the solid line.*

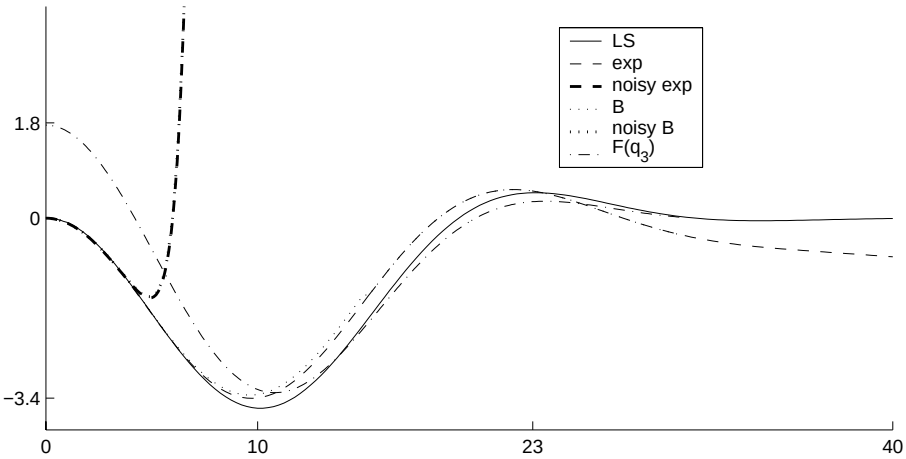

FIG. 9. *Profiles of the following radial and real-valued functions: scattering transform* $\mathbf{t}_3^{\mathrm{LS}}$ (*solid line*), *approximate scattering transforms* $\mathbf{t}_3^{\mathrm{B}}$ (*thin dotted line*) *and* $\mathbf{t}_3^{\exp}$ (*thin dashed line*), *and the Fourier transform* $\hat{q}_3(2|k|)$ (*dot-dash line*). *Also, plots of real parts of* $\tilde{\mathbf{t}}_3^{\mathrm{B}}(k)$ (*thick dotted line*) *and* $\tilde{\mathbf{t}}_3^{\exp}(k)$ (*thick dashed line*) *along positive* k_1 *axis.*

Then $\max|\gamma_3(x)| = 4$. Plots of γ_3 and the corresponding potential q_3 are found in Figure 2.

The functions $\mathbf{t}_3^{\mathrm{LS}}$, $\mathbf{t}_3^{\mathrm{B}}$, $\mathbf{t}_3^{\exp}$, $\tilde{\mathbf{t}}_3^{\mathrm{B}}$, and $\tilde{\mathbf{t}}_3^{\exp}$ were computed similarly to Example 1. See Figure 9 for a plot.

This example was considered in [59], where reconstructions of γ_3 from $\mathbf{t}_3^{\exp}$ and $\mathbf{t}_3^{\mathrm{LS}}$ were given. Reconstructions from $\mathbf{t}_3^{\mathrm{LS}}$, $\mathbf{t}_3^{\exp}$, and $\mathbf{t}_3^{\mathrm{B}}$ are included in Figure 10. Note that the reconstruction from $\mathbf{t}_3^{\mathrm{LS}}$ is indistinguishable from γ_3 in the plot. The reconstructions from noisy data are also included in Figure 10. Here $\tilde{\mathbf{t}}_3^{\exp}$ and $\tilde{\mathbf{t}}_3^{\mathrm{B}}$ were set to zero for $|k| > 3.5$. From the plots one observes that the reconstructions from noisy data have much lower amplitude and larger support than the actual γ_3. This may be due to the fact that these scattering transforms were truncated at a very small $|k|$ value such that the minimum value of $\mathbf{t}_3$ is not captured in the noisy approximation (as it was in the previous two examples).

We consider reconstructions of γ_3 from truncated $\mathbf{t}_3^{\mathrm{LS}}$ with $R = 13, 11, 9, 7$ and include the plots in Figure 11.

5.2. Second group: Asymmetric conductivity γ_4.

Example 4. Let F_ρ be given by (72) as for Example 2. Define

$$\gamma_4(x) := 1 + 4578\, F_{2/5}\left(x + \frac{1}{2}\right) - 1300\, F_{2/5}\left(x - \frac{1}{2}\right).$$

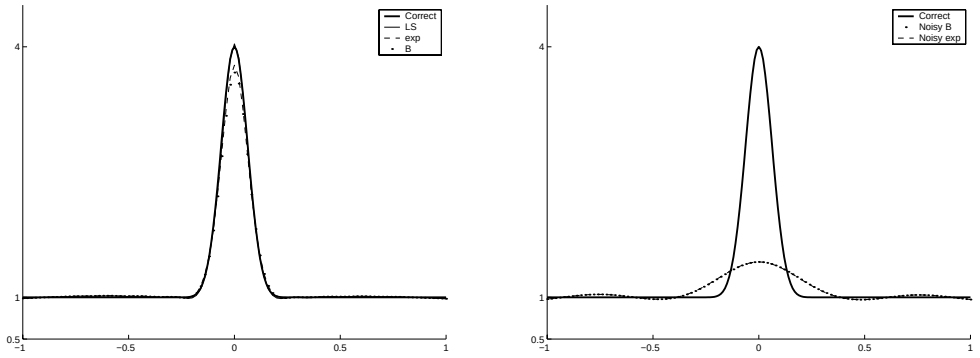

FIG. 10. *Profiles of the reconstructed conductivities for Example 3. The actual γ_3 is the thick solid line. The other plots denote reconstructions from $\mathbf{t}_3^{LS}$, $\mathbf{t}_3^{\exp}$, $\mathbf{t}_3^{B}$, $\tilde{\mathbf{t}}_3^{B}$, and $\tilde{\mathbf{t}}_3^{\exp}$.*

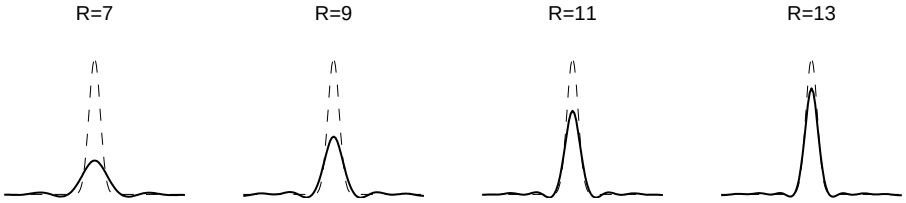

FIG. 11. *Profiles of reconstructions from truncated $\mathbf{t}_3^{LS}$. The actual γ_3 is the dashed line. The reconstruction is the solid line.*

Computation of the potential q_4 is done with finite difference approximation to the Laplace operator in the definition $q_4 = \gamma_4^{-1/2}\Delta\gamma_4^{1/2}$. See Figure 2 for plots of γ_4 and q_4.

The potential q_4 is difficult for numerical computations. It has sharp peaks that require fine sampling to be represented efficiently. This becomes evident in the computation of $\mathbf{t}_4^{\mathrm{LS}}$: we use the choice $M = 64$ (see section 3.1) in the square $[-35, 35]^2 \subset \mathbb{C}$. The accuracy is poor near $k = 0$ since $\mathbf{t}_4^{\mathrm{LS}}(0) \neq 0$. We refine the computation near the origin by using the choice $M = 256$ in the square $[-4, 4]^2 \subset \mathbb{C}$ resulting in more accurate computation. However, as evident in Figure 12, there is a visible jump between $\mathbf{t}_4^{\mathrm{LS}}$ values inside and outside the square $[-4, 4]^2$, indicating that the computation with $M = 64$ is not very accurate for $|k| = 4$.

In spite of these difficulties, the reconstructions are surprisingly accurate. Figure 13 contains plots of reconstruction from $\mathbf{t}_4^{\mathrm{LS}}$ (computed on the k-mesh $[-30, 30]^2$ with $h \approx 1.5$) and reconstructions from truncated $\mathbf{t}_4^{\mathrm{LS}}$ with $R = 20, 15, 12$ (computed on the k-mesh $[-20, 20]^2$ with $h \approx 1$). A reconstruction from $\mathbf{t}_4^{\mathrm{LS}}$ for x-values in the plane is found in Figure 14 with the actual conductivity found in Figure 15.

5.3. Third group: Distorted radial conductivities $\gamma_5, \gamma_6, \gamma_7$. These were obtained by composing our radially symmetric examples with a conformal map as described in section 3.4. See Figure 1 on page 1242 for the action of the conformal map.

Example 5. Define $\gamma_5 := \gamma_3 \circ \Psi^{-1}$. See Figure 2 for a plot of γ_5 and q_5.

We computed $\mathbf{t}_5^{\mathrm{LS}}(k)$ similarly to Example 4. We chose $M = 64$ in the square $[-35, 35]^2$ and $M = 256$ in the square $[-6, 6]^2$. Moreover, we computed $\mathbf{t}_5^{\exp}(k)$ in

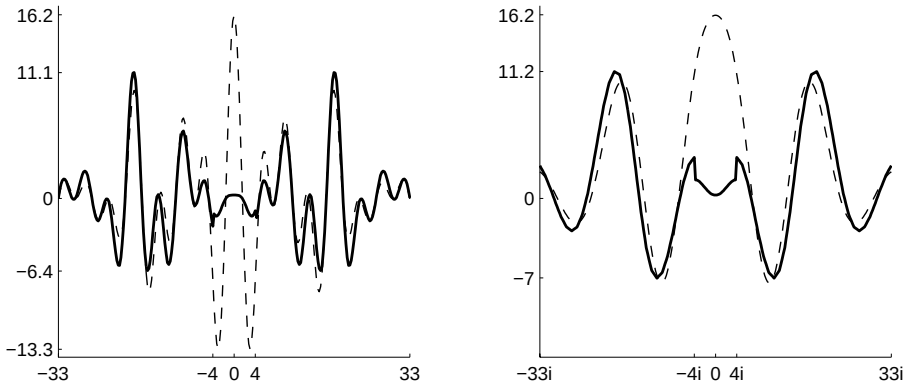

FIG. 12. *Plots of real parts of the scattering transform* $\mathbf{t}_4^{\mathrm{LS}}(k)$ (*thick solid line*) *and* $\hat{q}_4(-2k_1, 2k_2)$ (*dashed line*). *Note the jump at* $|k| = 4$ *caused by changing grid parameters to assure better accuracy near* $k = 0$.

FIG. 13. *Restrictions on* x_1 *axis of the reconstructions from truncated* $\mathbf{t}_4^{LS}$. *The actual* γ_4 *is the dashed line. The reconstruction is the solid line.*

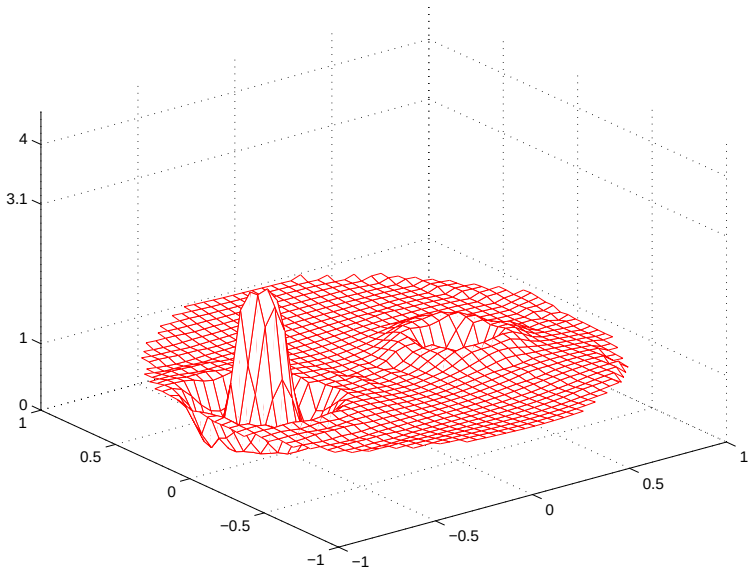

FIG. 14. *Reconstruction of* γ_4 *from* $\mathbf{t}_4^{LS}$.

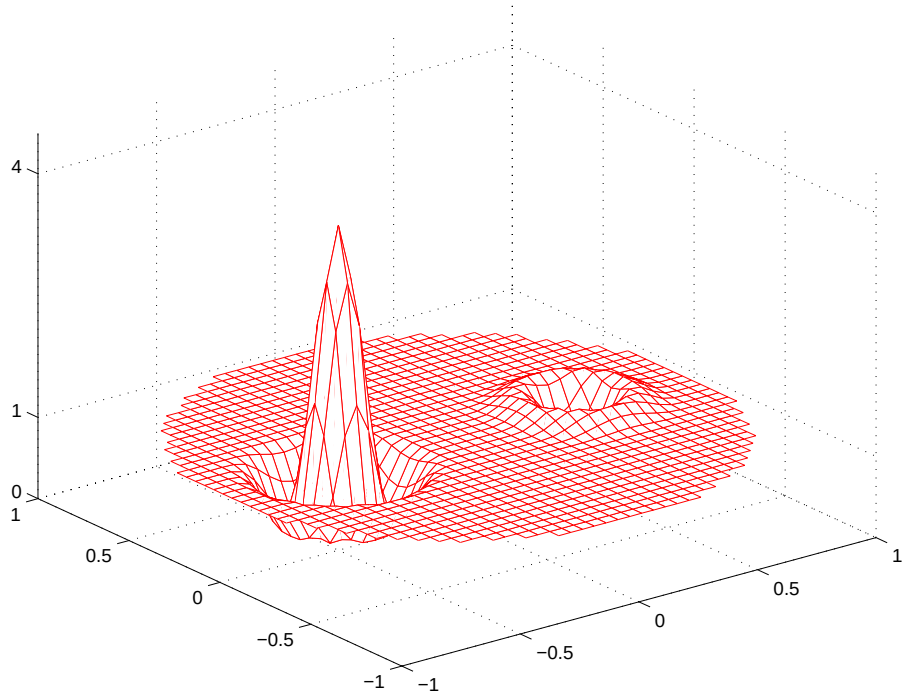

FIG. 15. *Actual conductivity* γ_4.

the square $[-35,35]^2$ as explained in section 3.4 using the 75 computed eigenvalues of Λ_{γ_3}. See Figure 16 for plots of real parts of $\mathbf{t}_5^{\mathrm{LS}}, \mathbf{t}_5^{\mathrm{exp}}$, and $\hat{q}_5$.

Reconstructions of γ_5 were obtained as above on the k-mesh $[-20,20]$ with $h \approx 1$. Cross-sectional plots of the reconstructions along the real axis are found in Figure 17. It is curious that in this example the reconstruction from $\mathbf{t}_5^{\mathrm{exp}}$ is more accurate than that from $\mathbf{t}_5^{\mathrm{LS}}$.

We consider reconstructions from truncated $\mathbf{t}_5^{\mathrm{LS}}(|k|)$ with $R = 15, 11, 9, 7$ and include the plots in Figure 18.

Example 6. Define $\gamma_6 := \gamma_2 \circ \Psi^{-1}$. See Figure 2 for a plot of γ_6 and q_6.

We computed $\mathbf{t}_6^{\mathrm{LS}}(k)$ similarly to Example 4. We chose $M = 64$ in the square $[-35,35]^2$ and $M = 256$ in the square $[-3,3]^2$. Moreover, we computed $\mathbf{t}_6^{\mathrm{exp}}(k)$ in the square $[-35,35]^2$ as explained in section 3.4 using the 75 computed eigenvalues of Λ_{γ_2}. See Figure 19 for plots of real parts of $\mathbf{t}_6^{\mathrm{LS}}, \mathbf{t}_6^{\mathrm{exp}}$, and $\hat{q}_6$.

Reconstructions of γ_6 were obtained as above. Cross-sectional plots of the reconstructions along the real axis are found in Figure 20 and reconstructions from truncated $\mathbf{t}_6^{\mathrm{LS}}(|k|)$ with $R = 9, 7, 5$ are found in Figure 21.

Example 7. Define $\gamma_7 := \gamma_1 \circ \Psi^{-1}$. See Figure 2 for a plot of γ_7 and q_7.

We computed $\mathbf{t}_7^{\mathrm{LS}}(k)$ similarly to Example 4. We chose $M = 64$ in the square $[-35,35]^2$ and $M = 256$ in the square $[-3,3]^2$. Moreover, we computed $\mathbf{t}_7^{\mathrm{exp}}(k)$ in the square $[-35,35]^2$ as explained in section 3.4 using the 75 computed eigenvalues of Λ_{γ_1}. See Figure 22 for plots of real parts of $\mathbf{t}_7^{\mathrm{LS}}, \mathbf{t}_7^{\mathrm{exp}}$, and $\hat{q}_7$.

Reconstructions of γ_7 were obtained as above. Cross-sectional plots of the reconstructions along the real axis are found in Figure 23. Plots of the conductivity in the plane are found in Figures 24 and 25. Reconstructions from truncated $\mathbf{t}_7^{\mathrm{LS}}(k)$ are

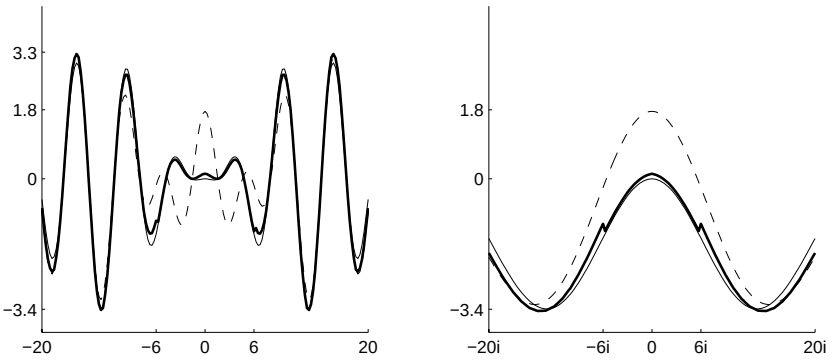

FIG. 16. *Plots of real parts of the scattering transform* $\mathbf{t}_5^{\mathrm{LS}}(k)$ (*thick solid line*), *the approximate scattering transform* $\mathbf{t}_5^{\exp}(k)$ (*thin solid line*), *and* $\hat{q}_5(-2k_1, 2k_2)$ (*dashed line*). *The left plot shows the profiles of the functions along* k_1 *axis and the right plot along* k_2 *axis. This figure illustrates three things. First, the computation is in accordance with the theoretical fact that* $\mathbf{t}_5^{\mathrm{LS}}(k) \approx \hat{q}_5(-2k_1, 2k_2)$ *for large* $|k|$. *Second,* $\mathbf{t}_5^{\exp}$ *is a reasonable approximation to* $\mathbf{t}_5^{\mathrm{LS}}$. *Third, the numerical computation of* $\mathbf{t}_5^{\mathrm{LS}}$ *becomes inaccurate near zero and the numerical computation of* $\mathbf{t}_5^{\exp}$ *becomes inaccurate for large* $|k|$.

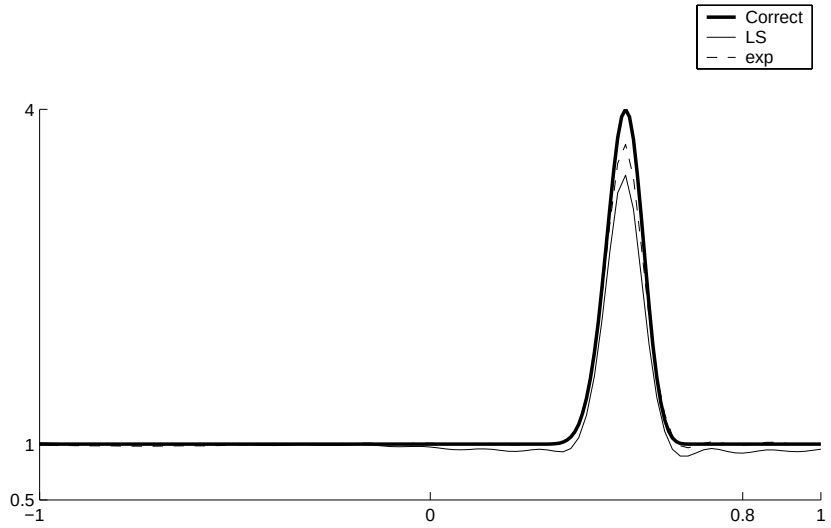

FIG. 17. *Restrictions to* x_1 *axis of the reconstructed conductivities for Example* 5. *The actual* γ_5 *is the thick solid line. The other plots denote reconstructions from* $\mathbf{t}_5^{LS}$ (*thin line*) *and* $\mathbf{t}_5^{\exp}$ (*dashed line*).

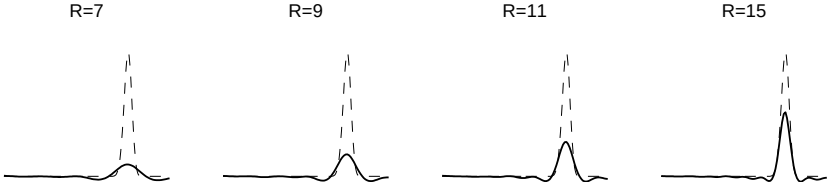

FIG. 18. *Restrictions to* x_1 *axis of reconstructions from truncated* $\mathbf{t}_5^{LS}$. *The actual* γ_5 *is the dashed line. The reconstruction is the solid line.*

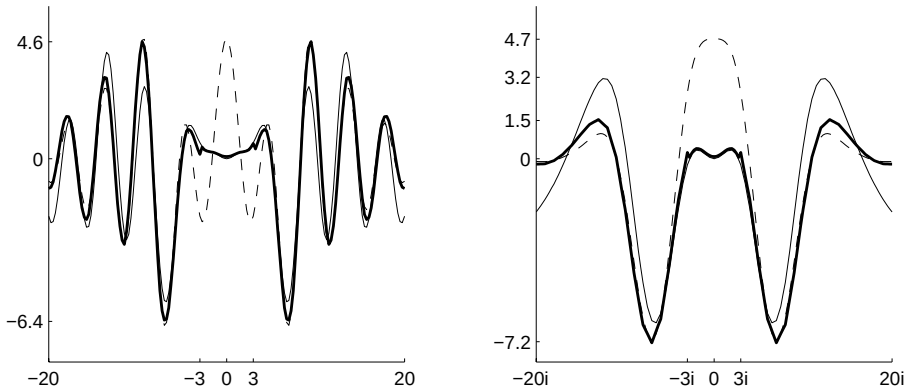

FIG. 19. *Plots of real parts of* $\mathbf{t}_6^{\mathrm{LS}}(k)$ (*thick solid line*), $\mathbf{t}_6^{\exp}(k)$ (*thin solid line*), *and* $\hat{q}_6(-2k_1, 2k_2)$ (*dashed line*). *The left plot shows the profiles of the functions along* k_1 *axis and the right plot along* k_2 *axis. The comments in the caption of Figure* 16 *apply here as well.*

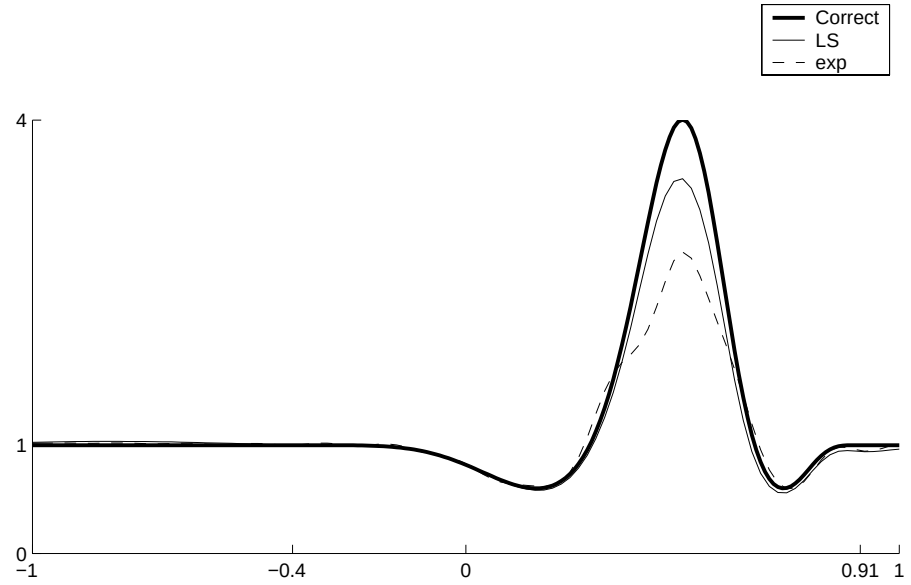

FIG. 20. *Restrictions to* x_1 *axis of the reconstructed conductivities for Example* 6. *The actual* γ_6 *is the thick solid line. The other plots denote reconstructions from* $\mathbf{t}_6^{LS}$ (*thin line*) *and* $\mathbf{t}_6^{\exp}$ (*dashed line*).

found in Figure 26. Although an R slightly larger than in Example 1 is needed to reconstruct the dip in the conductivity in this example ($R = 9$ as opposed to $R = 6$), significant information about the conductivity is recovered even when $R = 3$. This bodes well for the use of noisy data, since in our simulations the noisy scattering transforms were accurate for small k values.

6. Conclusion. We have shown by proofs and numerical experiments that Nachman's method can be used to reconstruct complicated features of conductivities from boundary data. We have presented two practical methods of computing the scat-

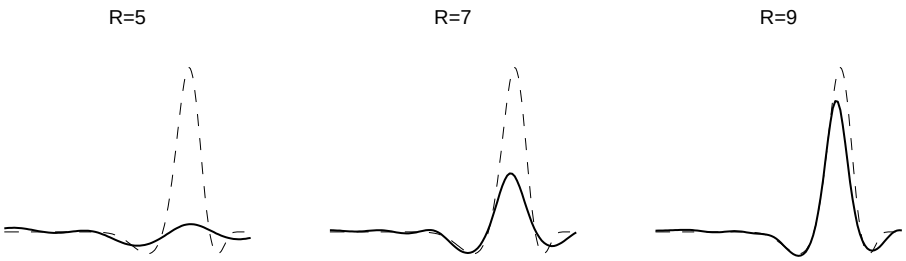

FIG. 21. *Restrictions to x_1 axis of reconstructions from truncated $\mathbf{t}_6^{LS}$. The actual γ_6 is the dashed line. The reconstruction is the solid line.*

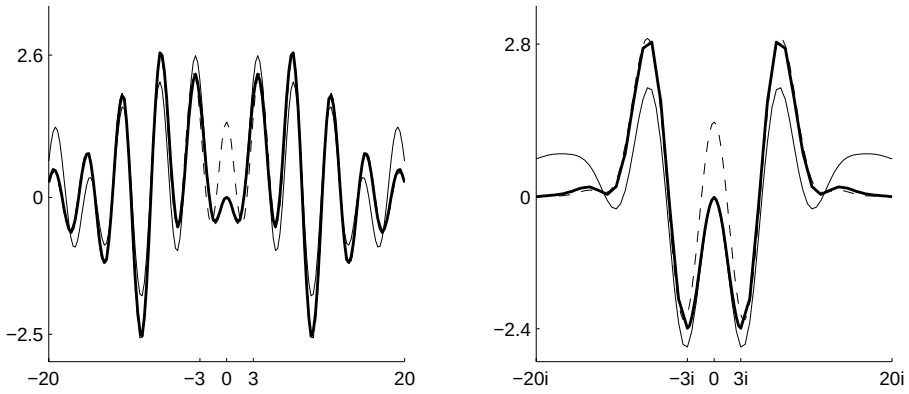

FIG. 22. *Plots of real parts of $\mathbf{t}_7^{\mathrm{LS}}(k)$ (thick solid line), $\mathbf{t}_7^{\exp}(k)$ (thin solid line), and $\hat{q}_7(-2k_1, 2k_2)$ (dashed line). The left plot shows the profiles of the functions along k_1 axis and the right plot along k_2 axis. The comments in the caption of Figure* 16 *apply here as well.*

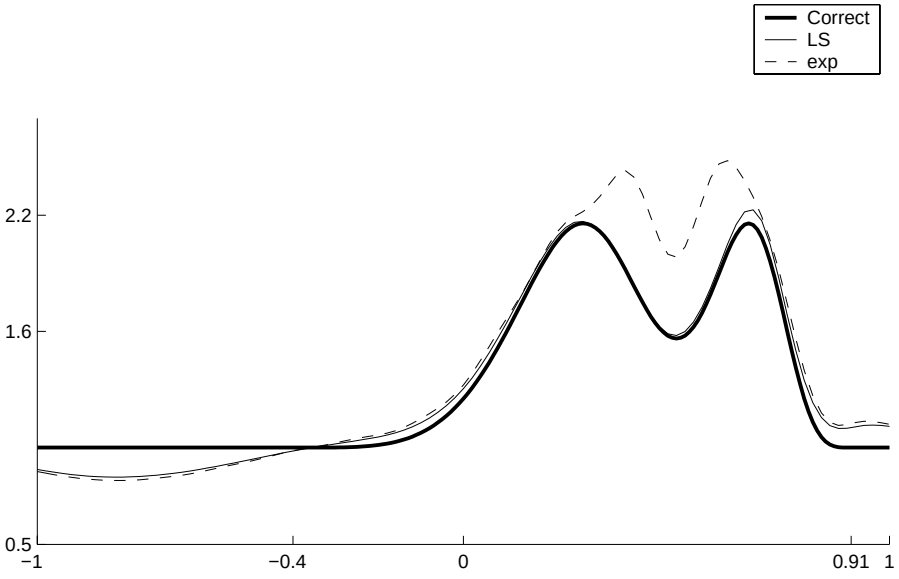

FIG. 23. *Restrictions to x_1 axis of the reconstructed conductivities for Example* 7. *The actual γ_7 is the thick solid line. The other plots denote reconstructions from $\mathbf{t}_7^{LS}$ (thin line) and $\mathbf{t}_7^{\exp}$ (dashed line).*

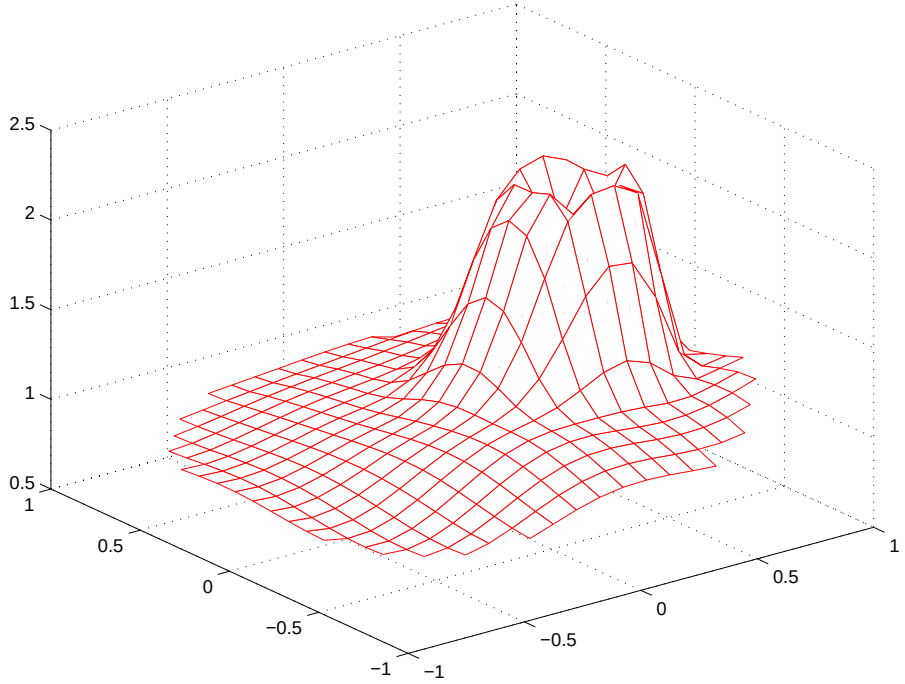

FIG. 24. *Reconstruction of* γ_7 *from* $\mathbf{t}_7^{LS}$.

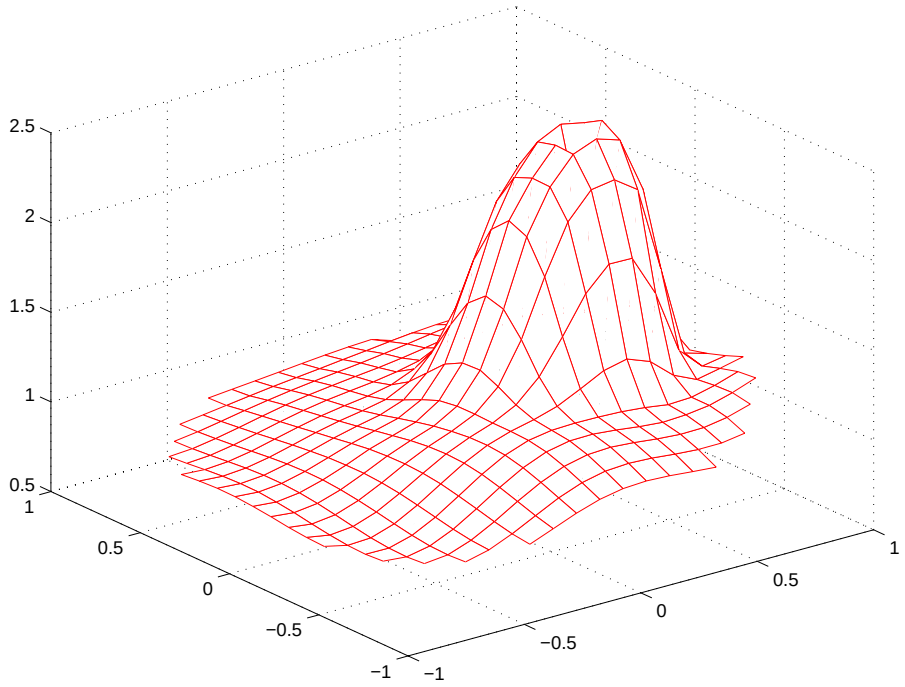

FIG. 25. *Reconstruction of* γ_7 *from* $\mathbf{t}_7^{\exp}$.

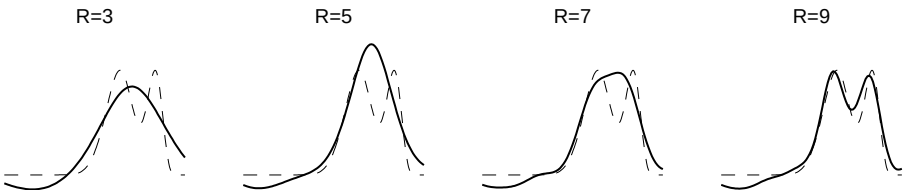

FIG. 26. *Restrictions to x_1 axis of reconstructions from truncated $\mathbf{t}_7^{LS}$. The actual γ_7 is the dashed line. The reconstruction is the solid line.*

tering transform from the Dirichlet-to-Neumann data. Both methods can be viewed as a regularization technique for the reconstruction algorithm. Reconstructions using the two regularized scattering transforms were computed for various symmetric and nonsymmetric examples for noisy and nonnoisy data and compared to reconstructions from the scattering transform computed from a known conductivity via the Lippmann–Schwinger-type equation. Both approximations led to reasonable reconstructions. The experiments give encouraging results for the practical use of this algorithm in EIT.

Acknowledgments. The authors thank Masaru Ikehata, David Isaacson, Matti Lassas, Adrian Nachman, Petri Ola, and Gennadi Vainikko for helpful discussions.

REFERENCES

[1] M. ABLOWITZ, D. BAR YAACOV, AND A. S. FOKAS, *On the inverse scattering transform for the Kadomtsev-Petviashvili equation*, Stud. Appl. Math., 69 (1983), pp. 135–143.
[2] R. A. ADAMS, *Sobolev Spaces*, Academic Press, New York-London, 1975.
[3] G. ALESSANDRINI, *Stable determination of conductivity by boundary measurements*, Appl. Anal., 27 (1988), pp. 153–172.
[4] G. ALESSANDRINI, *Singular solutions of elliptic equations and the determination of conductivity by boundary measurements*, J. Differential Equations, 84 (1990), pp. 252–273.
[5] A. ALLERS AND F. SANTOSA, *Stability and resolution analysis of a linearized problem in electrical impedance tomography*, Inverse Problems, 7 (1991), pp. 515–533.
[6] K. ATKINSON, *An Introduction to Numerical Analysis*, 2nd ed., John Wiley, New York, 1989.
[7] D. C. BARBER AND B. H. BROWN, *Applied potential tomography*, J. Phys. E. Sci. Instrum., 17 (1984), pp. 723–733.
[8] D. C. BARBER AND B. H. BROWN, *Progress in electrical impedance tomography*, in Inverse Problems in Partial Differential Equations, SIAM, Philadelphia, 1990, pp. 151–164.
[9] J. A. BARCELÓ, T. BARCELÓ, AND A. RUIZ, *Stability of the inverse conductivity problem in the plane for less regular conductivities*, J. Differential Equations, 173 (2001), pp. 231–270.
[10] R. BEALS AND R. COIFMAN, *Scattering, transformations spectrales et équations d'évolution non linéaires*, Goulaouic-Meyer-Schwartz Seminar 1980–1981 22, École Polytechnique, Palaiseau, France, 1981.
[11] R. BEALS AND R. COIFMAN, *Scattering, transformations spectrales et équations d'évolution non linéaires*. II, Goulaouic-Meyer-Schwartz Seminar 1981/1982 21, École Polytechnique, Palaiseau, France, 1982.
[12] R. BEALS AND R. R. COIFMAN, *Multidimensional inverse scattering and nonlinear partial differential equations*, A.M.S., 43 (1985), pp. 45–70.
[13] R. BEALS AND R. R. COIFMAN, *The d-bar approach to inverse scattering and nonlinear evolution equations*, Physica, 18 (1986), pp. 242–249.
[14] C. BERENSTEIN AND E. C. TARABUSI, *Inversion formulas for the k-dimensional Radon transform in real hyperbolic spaces*, Duke Math. J., 62 (1991), pp. 1–19.
[15] R. BLUE, *Real-Time Three-Dimensional Electrical Impedance Tomography*, Ph.D. thesis, R.P.I., Troy, NY, 1997.
[16] L. BORCEA, *Nonlinear Multigrid for Imaging Electrical Conductivity and Permittivity at Low Frequency*, Inverse Problems, 17 (2001), pp. 329–359.

[17] L. Borcea, J. G. Berryman, and G. Papanicolaou, *High contrast impedance tomography*, Inverse Problems, 12 (1996), pp. 835–858.
[18] L. Borcea, J. G. Berryman, and G. C. Papanicolaou, *Matching pursuit for imaging high-contrast impedance tomography*, Inverse Problems, 15 (1999), pp. 811–849.
[19] R. M. Brown and G. Uhlmann, *Uniqueness in the inverse conductivity problem for nonsmooth conductivities in two dimensions*, Comm. Partial Differential Equations, 22 (1997), pp. 1009–1027.
[20] A. P. Calderón, *On an inverse boundary value problem*, in Seminar on Numerical Analysis and its Applications to Continuum Physics, Soc. Brasil. Mat., Rio de Janeiro, 1980, pp. 65–73.
[21] S. Chanillo, *A problem in electrical prospection and an n-dimensional Borg-Levinson theorem*, Proc. Amer. Math. Soc., 108 (1980), pp. 761–767.
[22] M. Cheney, D. Isaacson, and E. L. Isaacson, *Exact solutions to a linearized inverse boundary value problem*, Inverse Problems, 6 (1990), pp. 923–934.
[23] M. Cheney, D. Isaacson, J. C. Newell, J. Goble, and S. Simske, *Noser: An algorithm for solving the inverse conductivity problem*, Internat. J. Imaging Systems and Technology, 2 (1990), pp. 66–75.
[24] M. Cheney, D. Isaacson, and J. C. Newell, *Electrical impedance tomography*, SIAM Rev., 41 (1999), pp. 85–101.
[25] W. Daily and A. Ramirez, *Electrical resistance tomography during in-situ tricholoethylene remediation at the savannah river site*, Appl. Geophys., 33 (1995), pp. 239–249.
[26] W. Daily, A. Ramirez, and R. Johnson, *Electrical impedance tomography of a perchloroethylene release*, JEEG, 2 (1998), pp. 189–201.
[27] W. Daily, A. Ramirez, D. LaBrecque, and J. Nitao, *Electrical resistivity tomography of vadose water movement*, Water Resources Res., 28 (1992), pp. 1429–1442.
[28] D. C. Dobson and F. Santosa, *An image-enhancement technique for electrical impedance tomography*, Inverse Problems, 10 (1994), pp. 317–334.
[29] O. Dorn, H. Berteta-Aguirre, J. G. Berryman, and G. Papanicolaou, *A nonlinear inversion method for 3D-electromagnetic imaging using adjoint fields*, Inverse Problems, 15 (1999), pp. 1523–1558.
[30] M. R. Eggleston, R. J. Schwabe, D. Isaacson, and J. C. Newell, *The application of electric current computed tomography to defect imaging in metals*, in Review of Progress in Quantitative NDE, Vol. 9A, Plenum Press, New York, 1989, pp. 455–462.
[31] L. D. Faddeev, *Increasing solutions of the Schrödinger equation,* Sov. Phys. Dokl, 10 (1966), pp. 1033–1035.
[32] A. S. Fokas and M. J. Ablowitz, *The inverse scattering transform for multidimensional* $2+1$ *problems*, in Nonlinear Phenomena, K. B. Wolf, ed., Lecture Notes in Physics, Springer, Berlin, 1984, pp. 137–183.
[33] M. Ikehata and S. Siltanen, *Numerical method for finding the convex hull of an inclusion in conductivity from boundary measurements,* Inverse Problems, 16 (2000), pp. 1043–1052.
[34] M. Ikehata and S. Siltanen, *Numerical Solution of the Cauchy Problem Using Faddeev's Green Function*, preprint.
[35] D. Isaacson and M. Cheney, *Effects of measurement precision and finite numbers of electrodes on linear impedance imaging algorithms*, SIAM J. Appl. Math., 15 (1991), pp. 1705–1731.
[36] V. Isakov, *Completeness of products of solutions and some inverse problems for PDE*, J. Differential Equations, 92 (1991), pp. 305–317.
[37] V. Isakov, *Uniqueness and stability in multi-dimesional inverse problems*, Inverse Problems, 9 (1993), pp. 579–621.
[38] V. Isakov, *Inverse Problems for Partial Differential Equations*, Springer, New York, 1998.
[39] D. S. Jerison and C. E. Kenig, *Boundary behaviour of harmonic functions in non-tangentially accessible domains*, Adv. Math., 46 (1982), pp. 80–147.
[40] J. Kaipio, V. Kolehmainen, E. Somersalo, and M. Vauhkonen, *Statistical inversion and Monte Carlo sampling methods in electrical impedance tomography*, Inverse Problems, 16 (2000), pp. 1487–1522.
[41] J. S. Kallman and J. G. Berryman, *Weighted least-squares methods for electrical impedance tomography*, IEEE Trans. Med. Imaging, 11 (1992), pp. 284–292.
[42] M. Klibanov, *A Newton-Kantorovich Method for Impedance Computed Tomography*, preprint.
[43] R. V. Kohn and A. McKenney, *Numerical implementation of a variational method for electrical impedance imaging*, Inverse Problems, 9 (1990), pp. 389–414.
[44] R. V. Kohn and M. Vogelius, *Determining conductivity by boundary measurements*, Comm. Pure Appl. Math., 37 (1984), pp. 289–298.
[45] R. V. Kohn and M. Vogelius, *Determining conductivity by boundary measurements* II. *Inte-*

rior results, Comm. Pure Appl. Math., 38 (1985), pp. 643–667.
[46] R. V. Kohn and M. Vogelius, *Relaxation of a variational method for impedance computed tomography*, Comm. Pure Appl. Math., 40 (1987), pp. 745–777.
[47] L. Liu, *Stability Estimates for the Two-Dimensional Inverse Conductivity Problem*, Ph.D. thesis, University of Rochester, Rochester, NY, 1997.
[48] J. L. Mueller, D. Isaacson, and J. C. Newell, *A reconstruction algorithm for electrical impedance tomography data collected on rectangular electrode arrays*, IEEE Trans. Biomed. Engr., 49 (1999), pp. 1379–1386.
[49] J. L. Mueller, D. Isaacson, and J. C. Newell, *Reconstruction of conductivity changes due to ventilation and perfusion from EIT data collected on a rectangular electrode array*, Physiol. Meas., 22 (2001), pp. 97–106.
[50] A. Nachman, *Inverse scattering at fixed energy*, in Proceedings of 10th International Congress on Mathematical Physics, K. Schmüdgen, ed., Springer–Verlag, Berlin, 1992, pp. 434–441.
[51] A. I. Nachman, *Reconstructions from boundary measurements*, Ann. of Math. (2), 128 (1988), pp. 531–576.
[52] A. I. Nachman, *Global uniqueness for a two-dimensional inverse boundary value problem*, Ann. of Math. (2), 143 (1996), pp. 71–96.
[53] A. Nachman and M. J. Ablowitz, *A multi-dimensional inverse scattering method*, Stud. Appl. Math., 71 (1984), pp. 243–250.
[54] A. I. Nachman, J. Sylvester, and G. Uhlmann, *An n-dimensional Borg-Levinson theorem*, Comm. Math. Phys., 115 (1988), pp. 595–605.
[55] R. G. Novikov and G. M. Khenkin, *The $\bar{\partial}$-equation in the multidimensional inverse scattering problem*, Uspekhi Mat. Nauk., 42 (1987), pp. 93–152.
[56] A. Ramirez, W. Daily, D. LaBrecque, E. Owen, and D. Chesnut, *Monitoring an underground steam injection process using electrical resistance tomography*, Water Resources Research, 29 (1993), pp. 73–87.
[57] A. Ramirez, W. Daily, A. Binley, D. LaBrecque, and D. Roelant, *Detection of leaks in underground storage tanks using electrical resistance methods*, J. Envir. Eng. Geophys., 1 (1996), pp. 189–203.
[58] F. Santosa and M. Vogelius, *A backprojection algorithm for electrical impedance imaging*, SIAM J. Appl. Math., 50 (1990), pp. 216–243.
[59] S. Siltanen, J. Mueller, and D. Isaacson, *An implementation of the reconstruction algorithm of A. Nachman for the 2-D inverse conductivity problem,* Inverse Problems, 16 (2000), pp. 681–699.
[60] S. Siltanen, J. Mueller, and D. Isaacson, *Errata: An implementation of the reconstruction algorithm of A. Nachman for the 2-D inverse conductivity problem,* Inverse Problems, 17 (2001), pp. 1561–1563.
[61] S. Siltanen, J. Mueller, and D. Isaacson, *Reconstruction of high contrast 2-D conductivities by the algorithm of A. Nachman,* in Radon Transforms and Tomography, E. T. Quinto, L. Ehrenpreis, A. Faridani, F. Gonzalez, and E. Grinberg, eds., AMS, Providence, RI, 2001, pp. 241–254.
[62] S. Siltanen, *Electrical Impedance Tomography and Faddeev Green's Functions*, Ph.D. thesis, Helsinki University of Technology, Helsinki, 1999.
[63] E. Somersalo, M. Cheney, D. Isaacson, and E. Isaacson, *Layer stripping: A direct numerical method for impedance imaging,* Inverse Problems, 7 (1991), pp. 899–926.
[64] S. Stphanesci, C. Schlumberger, and M. Schlumberger, *Sur la distribution electrique autour d'une prise de terre ponctuelle dans un terrain a couches horizontales, homogenes et isotropes*, J. Physics and Radium Ser., 7 (1930), pp. 132–140.
[65] Z. Sun, *On an inverse boundary value problem in two dimensions*, Comm. Partial Differential Equations, 14 (1989), pp. 1101–1113.
[66] Z. Sun, *The inverse conductivity problem in two dimensions*, J. Differential Equations, 87 (1990), pp. 227–255.
[67] Z. Sun and G. Uhlmann, *Generic uniqueness for an inverse boundary value problem*, Duke Math. J., 62 (1991), pp. 131–155.
[68] A. J. Suroviec, S. S. Stuchly, J. R. Barr, and A. Swarup, *Dielectric properties of breast carcinoma and the surrounding tissues*, IEEE Trans. Biomed. Eng., 35 (1988), pp. 257–263.
[69] A. Swarup, S. S. Stuchly, and A. Surowiec, *Dielectric properties of mouse mca*l *fibrosarcoma at different stages of development*, Bioelectromagnetics, 12 (1991), p. 108.
[70] J. Sylvester, *A convergent layer stripping algorithm for the radially symmetric impedance tomography problem*, Comm. Partial Differential Equations, 17 (1992), pp. 1955–1994.
[71] J. Sylvester and G. Uhlmann, *A uniqueness problem for an inverse boundary value problem in electrical prospection*, Comm. Pure Appl. Math., 39 (1986), pp. 91–112.

[72] J. Sylvester and G. Uhlmann, *A global uniqueness theorem for an inverse boundary value problem*, Ann. of Math. (2), 125 (1987), pp. 153–169.
[73] J. Sylvester and G. Uhlmann, *Inverse boundary value problems at the boundary – continuous dependence*, Comm. Pure Appl. Math., 41 (1988), pp. 197–219.
[74] J. Sylvester and G. Uhlmann, *The Dirichlet to Neumann map and applications*, in Inverse Problems in Partial Differential Equations, Philadelphia, SIAM, 1990, pp. 101–139.
[75] G. Vainikko, *Fast solvers of the Lippmann-Schwinger equation*, in Direct and Inverse Problems of Mathematical Physics (Newark, DE), Int. Soc. Anal. Appl. Comput. 5, Kluwer Academic Publishers, Dordrecht, The Netherlands, 2000, pp. 423–440.
[76] A. Wexler, B. Fry, and M. Neuman, *Impedance computed tomography algorithm and system*, Appl. Opt., 24 (1985), pp. 3982–3985.
[77] R. A. Williams and M. S. Beck, eds., *Process Tomography-Principles, Techniques, and Applications*, Butterworth–Heinemann, Oxford, UK, 1995.
[78] C. G. Xie, S. M. Huang, and B. S. Boyle, *Electrical capacitance tomography for flow imaging: System model for development of image reconstruction algorithms and design of primary sensors*, IEE Proceedings, Part G, Circuits, Devices and Systems, 139 (1992), pp. 89–98.
[79] T. J. Yorkey, J. G. Webster, and W. J. Tompkins, *Comparing reconstruction algorithms for electrical impedance tomography*, IEEE Trans. Biomed. Eng., 34 (1987), pp. 843–852.